POLITECNICO DI MILANO
POLO REGIONALE DI LECCO
Facoltà di Ingegneria Industriale

Corso di Laurea in Ingegneria Meccanica

(Master's Degree in Mechanical Engineering)

Feasibility analysis of miniaturized FTIR spectrometer for ExoMars mission.

Supervisor: Prof. Bortolino SAGGIN
Ass.Supervisors: Ing. Diego SCACCABAROZZI

Master's thesis of:

Irina SHATALINA Matr. 737631

Academic Year 2009 - 2010

Index

Figures list

Tables list

Drawings list

Abstract

The objective of this work is to design an Infra-Red Fourier Spectrometer (IRFS) for the ESA mission "ExoMars 2016". This instrument, called micro-MIMA (micro-Martian Infra-red Mapper), will be mounted on a descending module to Mars and will observe the Martian atmosphere after landing. One goal is to study the features of atmosphere gas-composition (analysis of methane presence in particular) to make conclusions about possible biological activity and to check the meteorological conditions at the landing site.

So long, the instrument will measure the atmosphere spectrum with the resolution necessary to identify its gas content by recognizing spectral features of each element.

Design constraints for the mission are quite strict:

- limited mass, size and power budget;
- high stress resistance for the landing shock*;
- withstanding of severe environmental conditions without any power for thermal control)*;
- resistance for strong vibrations of the high acceleration levels in wide frequency range*.

Model design is supported by the finite element analysis simulating the static and dynamic loads during launch and landing of the system, as well as thermo-elastic analysis for the thermal field during operating process (including thermal stresses and instrument misalignments computation).

The final result of this work is the design of an instrument mock-up for further performance characteristics check. This mock up will be simplified from the structural point of view but with detailed representation of mounting, regulation and positioning of optical elements and piezoactuator group.

**Note: as exact mechanical constraints and environment conditions for this mission are not defined yet, as base will be taken requirements for 2018 Exo-Mars Pasteur Mission; following those constraints micro-MIMA in case of necessity can be mounted on the Rover mast as well.*

Substantial summary in Italian

L' obiettivo di questo lavoro è la progettazione di micro-MIMA, spettrometro infrarosso di Fourier per la missione ESA "ExoMars 2016". Lo strumento sarà montato su un modulo di discesa su Marte e dopo l'atterraggio, osserverà l'atmosfera marziana al fine di studiarne la composizione ottenendo informazioni utili per la successiva missione ESA in programma nel 2018-2019.

Il design del modello è stato supportato da analisi agli elementi finiti simulando i carichi statici e dinamici durante le fasi di lancio e atterraggio del sistema. Inoltre si è realizzato un modello termo-elastico dello strumento con l'obiettivo di ricavare la distribuzione delle temperature e calcolare il disallineamento introdotto.

Il risultato finale è la progettazione di un modello dimostrativo dello strumento al fine di verificare le caratteristiche operative e le prestazioni attese.

Chapter 1

Introduction

Fourier transform spectroscopy is a technique to obtain high resolution spectra of the light. The main element of the Fourier spectrometer is the interferometer which gives an interferogram of the observed radiation. Here we describe the working principle of the Fourier spectrometer, pointing out its application for the micro-MIMA, as well as provide the general description of the overall ESA space mission "ExoMars 2016". Further explanation of the micro-MIMA instrument scientific objectives, construction, design constraints and technical requirements will be mentioned.

1.1 FTS working principle

Fourier Transform Spectrometer (FTS) working principle is based on the Michelson interferometer. The last one consists of light source, 2 mirrors (fixed and moving ones), half-transparent mirror (beam splitter) at the 45° angle, which divides the coming beam into two perpendicular rays with 50% intensity, and a sensor (Fig. 1.1). (Notice that beam splitter is equally spaced from both mirrors.)

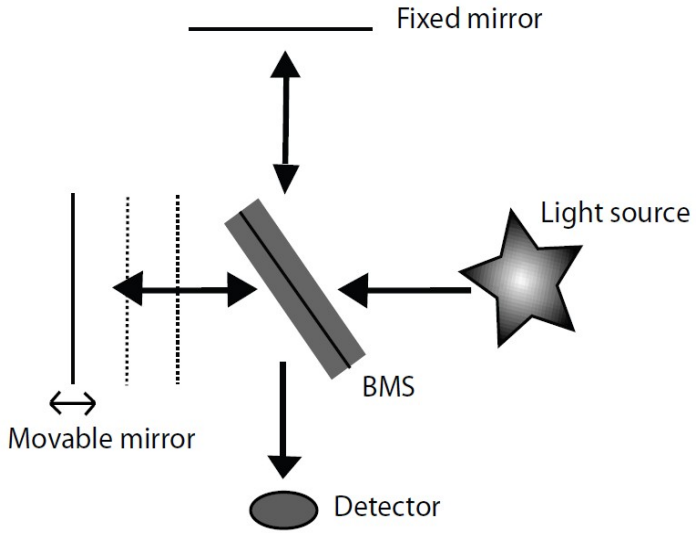

Fig. 1.1 Michelson interferometer scheme

If consider ways of two secondary beams, it is easy to see that the difference between their travelling distances will affect interference picture on the detector due to optical retardation. In case equal distance these beams will be in-phase coherent creating the constructive interference.
By shifting the moving mirror we can change this distance and thus the interference picture. For example the mirror shift of ¼ λ provides the ½ λ optical retardation and thus the total destructive interference on the detector. So far optical retardation of integer number of wavelength provides the maxima, while half-integer – total minima. Thus interferogram depends on the wavelength of the monochromatic light, while simultaneous usage of two different wavelengths results in the superposition of interference pictures for each singular wavelength.
So the optical retardation created by movement of mirrors affects on the interference in the interferometer as it would do a shutter opening/closing the light beam periodically. The frequency of those switches from dark (destructive interference) to light (constructive interference) is so-called Fourier frequency and it can be easily calculated while knowing the moving mirror velocity and the wavenumber. So with a monochromatic source the intensity on the detector will follow the cycle from max to min value (Fig. 1.2).

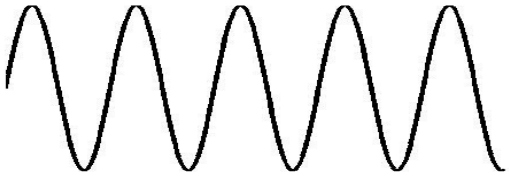

Fig. 1.2 Simulated interferogram of the monochromatic input

As was said before the broadband light source will provide the superposition of the interferences for each wavelength in the final interferogram (intensity vs. optical path difference). This interferogram (Fig. 1.3 A) by means of FFT techniques is transformed to the original spectrum (intensity vs. wavelength) of radiation (Fig. 1.3 B).

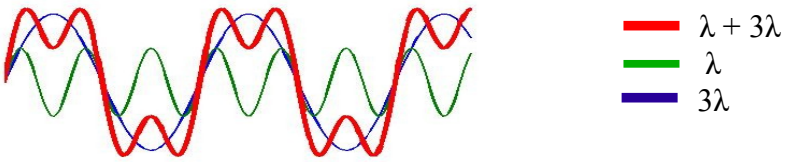

A

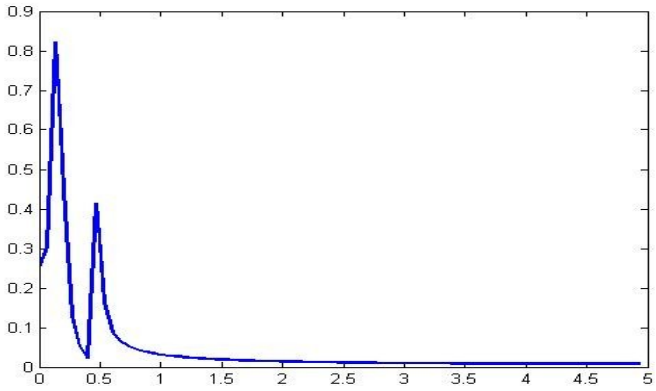

B

Fig. 1.3 Broadband light input (A – superposition for different wavelength inputs; B – simulated spectra)

Planar mirrors in the classical Michelson interferometer might be substituted by the cubic corner reflectors (Fig. 1.4). The working principle is the same (incoming light beam is divided in two, reflected on mirrors and an interferogram is obtained on the detector). In this case the optical retardation is provided by the rotation of both mirrors around the pendulum axis.

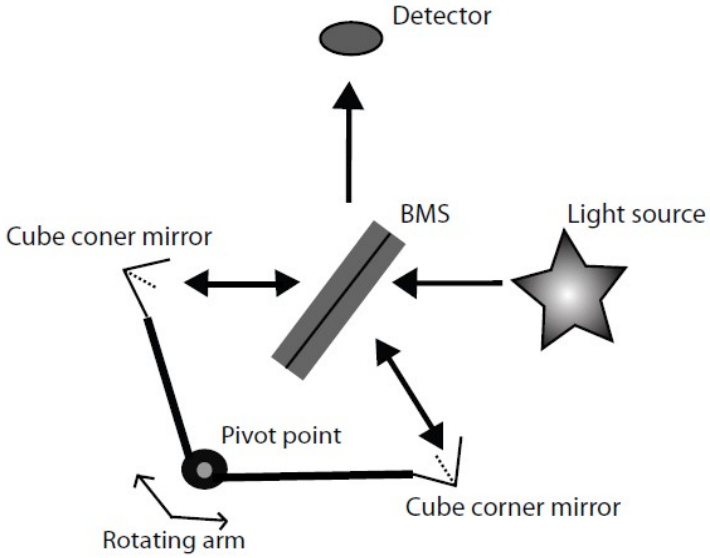

Fig. 1.4 Double pendulum interferometer scheme

Last configuration has a list of advantages comparing with the classical scheme:

- usage of rotation movement instead of translation is more preferable in terms of tolerances (realization of usual bearing system is much easier than one of a linear guide);
- this configuration appears to be more compact for the mass and volume constraints.

1.2. Aurora Programme: ExoMars missions.

The ESA Directorate of Human Spaceflight, Microgravity and Exploration developed the Aurora Programme in order to perform the future exploration of the Solar System using robot systems as well as human crews. Plan of Aurora consists of the several robotic missions, each well technologically equipped and ready to act as an independent building block (to ensure possible human presence in the exploration process). First goals to be investigated are Mars and Moon, then probably other near earth objects.
ExoMars programme is 1st in these series of missions. It is supposed to create the base for further exploration activities of ESA, with the fundamental scientific task as the main goal: search for extinct or extant life.
It is divided into following 2 subsequent missions:

- one mission under ESA lead, launched in 2016 by a US launcher including a joint US-European Orbiter releasing a European EDL demonstrator;
- another mission under NASA lead, launched in 2018 by a US launcher including a European Rover and a US Rover both deployed by a US EDL system.

1.2.1. "ExoMars 2016: Orbiter and EDL demonstrator".

ExoMars 2016 mission shall accomplish the following objectives:

- *Technological objective*: Entry, Descent and Landing (EDL) of a payload on the surface of Mars;
- *Scientific objective*: to investigate Martian atmospheric trace gases and their sources;
- *Communication objective*: provide communications capability for present and future ESA/NASA missions (2018-2020).

ESA will design, build and integrate a large Spacecraft Composite consisting of an ESA Orbiter which will carry the scientific trace gas payload instrumentation and an ESA EDL Demonstrator. The Spacecraft Composite will be launched in early January 2016 by a NASA and will arrive at Mars approximately 9 months later in mid-October of 2016. Prior to arrival at Mars the ESA EDL Demonstrator will be released from the ESA Orbiter and will enter the Mars

atmosphere from a hyperbolic arrival trajectory. The release of the EDL Demonstrator will take place 3-5 days prior to the critical Mars Orbit Insertion manoeuvre by the ExoMars Orbiter. The sequence of manoeuvres following the separation will be designed to maximise the chance of receiving the UHF radio beacon signals from the EDL Demonstrator during its Entry, Descent and Landing phase. Subsequently, the ExoMars Orbiter will begin a series of manoeuvres to arrive at the science and communications orbit with an altitude in the range of 350 Km to 420 Km. The science operations phase is expected to begin at the earliest in May of 2017 (depending on the actual duration of the aerobraking phase) and last for a period of one Martian year.

European Orbiter

The Exomars Orbiter (Fig. 1.5) is built around the Spacebus telecommunication platform from TAS-F with an avionic module (or service module) located on the basis of the platform and a primary structure built around an 1194 mm central tube. The dry mass of the Orbiter is about 1000kg.The nominal lifetime of the system is 7 years so the Orbiter will be operational till end of 2022, assuming its launch to be performed in January 2016.
The Orbiter configuration provides space to accommodate all science Instruments, in the area of the –Y panel also called Mars Nadir face (Fig. 1.5 A) and the +X panel looking at the cold space during the Mars orbit science phase (Fig. 1.5 B).

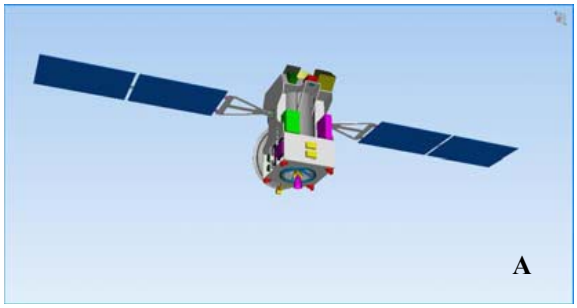

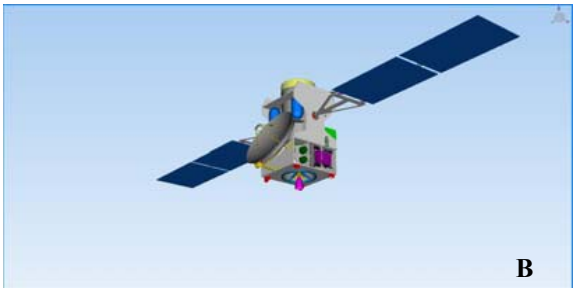

Fig. 1.5 ExoMars 2016 European Orbiter (A - NADIR face with potential science Instruments; B - Anti-Nadir face with HGA for X-band communication with Earth)

The total maximum mass allocated for all of the instruments is 125 kg. They shall be mounted on one of two mounting planes (Fig. 1.6).

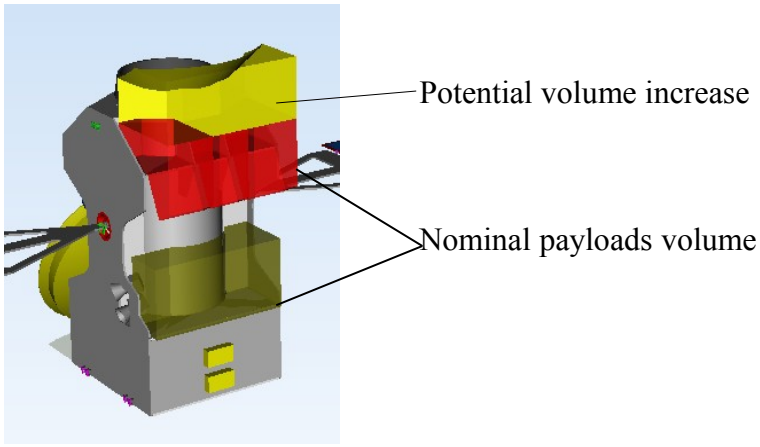

Fig. 1.6 Spacecraft structure with payloads volumes

Payload will include set of instruments to achieve following main scientific objectives of the mission:

- Detection of a broad suite of atmospheric trace gases
- Characterization of their spatial and temporal variation
- Localization of source of key trace gases

European EDL demonstrator

The EDL Demonstrator (Fig. 1.7) will provide Europe with the technology of landing on the surface of Mars with a controlled landing orientation and touchdown velocity. The design maximises the use of technologies already in development within the ExoMars programme.
These technologies include:

- Thermal Protection System Material
- Parachute System
- Radar Doppler Altimeter
- Liquid propulsion controlled final braking

The configuration of the ESA EDL Demonstrator will include engineering sensors for system performance evaluation during EDL phase. As the arrival of the Demonstrator might contemporize Mars Global Dust Storm so all system will be designed to survive such severe environment.

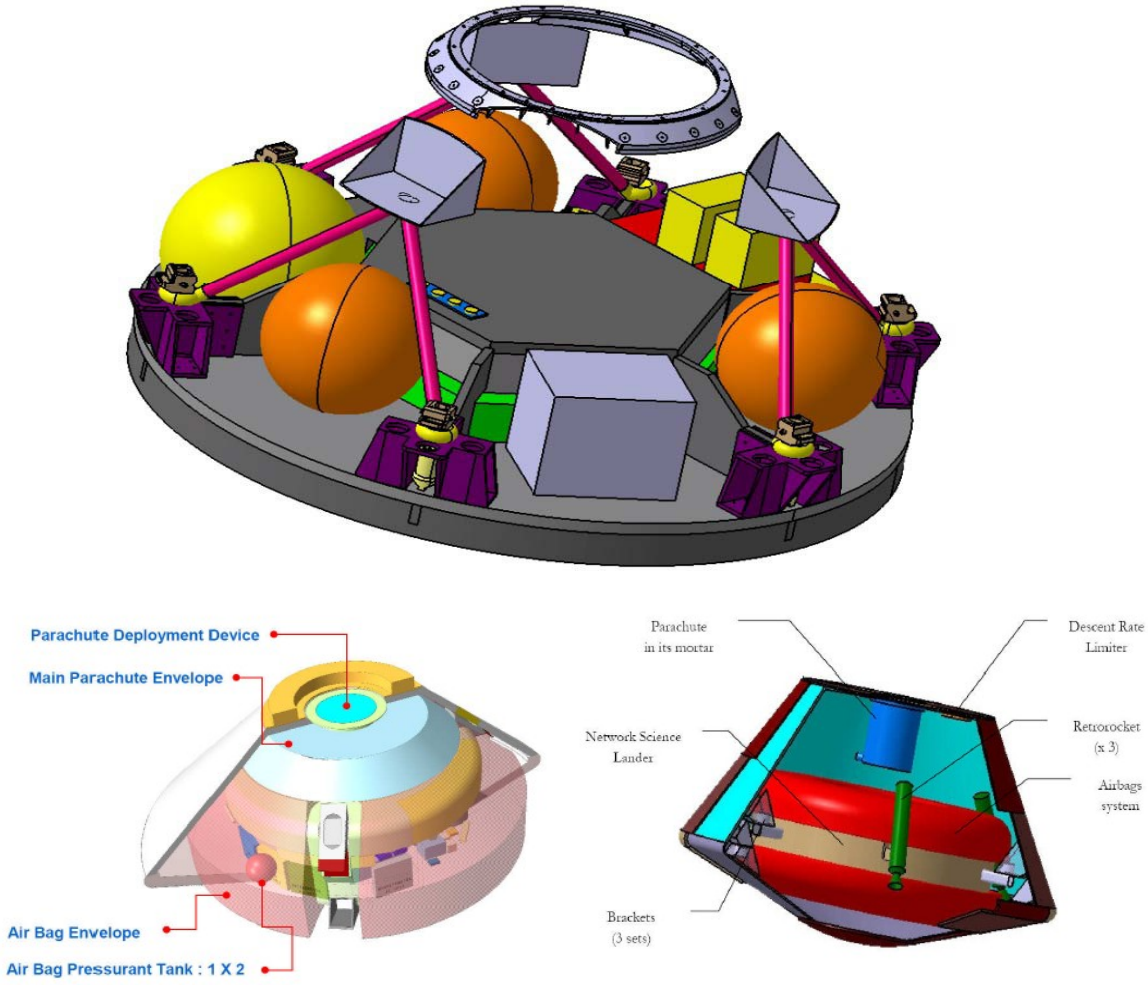

Fig. 1.7 ExoMars 2016 European EDL Demonstrator

After entry a single stage Disk Gap Band parachute will be deployed and the landing process will be controlled by closed-loop Guidance, Navigation and Control (GNC) system consisting of Radar Doppler Altimeter sensor and on-board Inertial Measurement Units (for liquid propulsion system).
The EDL Demonstrator is expected to survive on the surface of Mars for a short time by using the excess energy capacity of its primary batteries. So it will be equipped by the specific Instrumental Payload which will gather information about Martian atmosphere and environment conditions using available resources of Demonstrator without adding any additional systems for solar power

generation or for thermal control. The final list of those instruments is not defined yet; conceivably it will include camera, measuring means for wind speed value, dust content, humidity and atmosphere pressure, ***IRFS micro-MIMA***.

1.2.2. "ExoMars 2018: Rover and Pasteur Payload"

Main scientific objectives of ExoMars2018 (listed in order of priority) are:

- search for any evidence of present/past life on Mars;
- acquire 3-dimensional water/geochemical environment of Mars surface;
- evaluation of the conditions for further human missions;
- subsurface and deep interior of the planet investigation (to make conclusions about habitability and evolution of Mars).

The ExoMars 2018 payload instrumentation will be located on two different vehicles: Pasteur payload – on the moving Rover (Fig. 1.8), Geophysics and Environment Package (GEP) Payload – on the fixed station (which also will perform functions of the lander of the rover). Rover Payload will follow 1st two of the named goals. It will be autonomic for regional mobility of several kilometers using solar energy as the power source.

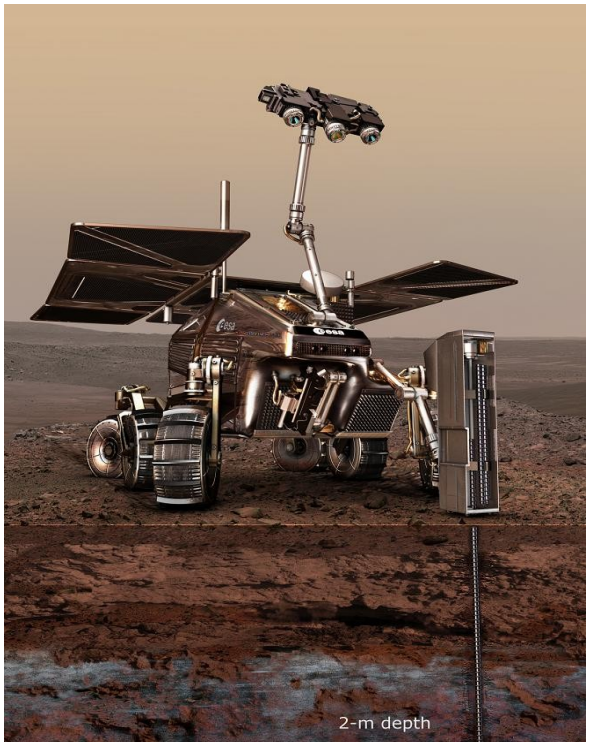

Fig.1.8 ExoMars 2018 Pasteur Rover

1.3. Micro-MIMA.

Micro-MIMA is a double pendulum Fourier Transform Spectrometer as well, with additional optical system to assure the atmosphere observation of roundly 140° FOV.

1.3.1.Objectives

Micro-MIMA is designed to be accommodated on mounting deck on the top of the European EDL Demonstrator of ExoMars 2016 mission. In cooperation of the other instruments of the payload it will aim to achieve main scientific results. In particular will follow goals study of the planet atmosphere in order to collect information about its gas-composition (in particular methane presence) to make conclusions about possible biological activity and to check the meteorological conditions at the landing site.

So on micro-MIMA will detect presence and concentration of the following CH_4, H_2O, N_2O, SO_2, CO, O_3 and other molecules.

Peculiar attention on the methane component is caused by the fact that its presence in Martian atmosphere has been firstly identified by observation of the Planetary Fourier Spectrometer but is still to be confirmed by other instruments. Hypothetical reasons for methane existence are either biological or related to Mars ancient volcanic activity. Both of those origins are not compatible with the present conception of Martian environment.

To validate the results provided by micro-MIMA its readout can be compared with one of the SFTIR (Solar Fourier Transform IR Spectrometer, mass about 25 kg) mounted on the European Orbiter (which measures the spectrum of sun passing through the atmosphere at limb: broad survey of trace gases with high precision).

1.3.2. Elements

Micro-MIMA consists of two main layouts: optical and mechanical.
Optical one, calculated and designed by the IFSI-INAF researchers, includes:

- entrance optics (first optics on the way of incoming radiance, gathers it from all directions on the spherical surface and brings it to the subsequent optic element – beam splitter – as a beam of parallel rays);
- beam splitter (divides the beam into 2 parts of about 50% intensity inside the interferometer);

- cubic corner reflectors (reflect the beam and send it back to the beam splitter; their relative movement creates the optical path difference that affects on the interferogram obtained);
- focusing lens (focuses the incoming beam on the detector);
- reference laser group;
- infrared photodetector.

The goal of this work is designing the mechanical layout which consists of:

- double pendulum mechanism (is mounted on the c-flex bearings system and holds the cubic reflectors);
- instrument frame (where all elements are located);
- piezoactuator group(to perform the rotation of the pendulum system);
- blocking element (ensures position of the pendulum during launch/landing shocks).

More details about optimisation of micro-MIMA configuration will be given later in this work.

1.3.3. Working principle

Working principle is based on one of the double pendulum interferometer with corner cubes (Fig. 1.9) which has been successfully implemented in similar instruments designed and qualified for Mars Express (PFS) and Venus Express. Micro-MIMA is designed to measure spectrum with resolution of 2 cm^{-1}.

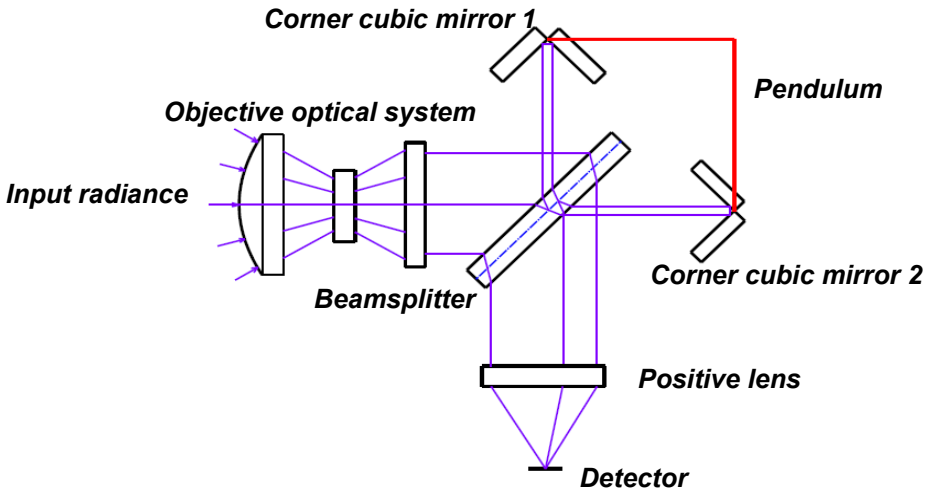

Fig. 1.9 Micro-MIMA optical scheme

To understand better the working principle of the instrument here is given then general explanation of the interferogram acquisition process. To acquire the incoming radiance at constants OPD steps reference laser is used; it's spatial frequency is doubled maximum observed one, and it follows the same path as an observed beam inside the interferometer. A special sensor measures the laser interferogam, and its zeros are used as a trigger for acquisition system.

Also the instrument meets another problem: in the acquired interferogram there always are present some disturbances due to vibrations, electronics noise, etc, thus providing some spectrum distortions. Those distortions must be identified and eliminated by usage of post processing of acquired data.

1.3.4. Functional requirements

Following the scientific purposes the instrument is designed to measure atmosphere spectra with resolution sufficient to identify its gas content by analysis spectral features of the acquired interferogram.
For that purpose next functional requirements are listed:

- spectral range 2.0-5 μm wavelength (2000 – 5000cm^{-1} wavenumber);
- spectral resolution 2 cm^{-1} (leaving possibility for 1 cm^{-1});
- entrance optics FOV 140°;
- instrument FOV 1,8°;
- max optical path difference 5mm (±2,5 mm double sided interferogram, leaving possibility for ±5 mm OPD in case spectral resolution of 1 cm^{-1});
- single PbSe detector;
- overall mass budget including electronics 250 g (note: max excess of 10%) with estimated quota of 50 g for instrument itself.

1.3.5.Environmental conditions

Environmental conditions predicted for ExoMars 2018 Payload (and so as well extended for micro-MIMA) are following: non working temperature varies around -100÷120°C, while operative one goes at level about -70°C. This would result in thermo-elastic stresses which have to be accounted for the interferometer design. As the power budget is quite limited there is no thermal control system proposed for the instrument. So a proper thermal insulation system has to be designed for the instrument.
At the same time detector and reference laser diode have to be heated up to and -60 ÷ -30°C (with accuracy of 0.3°C laser and of 1°C for detector).

Comparing with Earth Mars environment is affected by higher levels of radiation:

- total ionizing radiation 2.5 krad (for 4 mm aluminum shielding);
- non-ionizing energy loss 5 10^7 MeV/g (for 4 mm aluminum shielding).

It comes out that all the materials used in the micro-MIMA should be insensitive for the above levels of radiation.

1.3.6. Dynamic loads

Up to now dynamic loads for micro-MIMA are not defined, so we have taken them from the ExoMars 2018 payload requirements [3]:

- **landing load**: a quasi-static acceleration of 1000 m/s^2 related to the shock of landing on Mars surface;
- **sweep sine**: vibrations in a frequency range of 30-100 Hz;
- **random excitation**: an rms acceleration value of 170 m/s^2 spread in a frequency range between 20-2000 Hz.

Chapter 2

Structural design

This chapter is devoted to micro-MIMA mechanical design and thermoelastic analysis predicting instrument response to the mechanical and thermal loading conditions.

2.1 Mechanical design

This part of chapter is devoted to the instrument mechanical design. Instrument behaviour under static and dynamic loads (during take off from Earth and landing on Mars surface) has been investigated by means of FEM simulations performed on a simplified model. In order to proceed to the detailed design of micro-MIMA, loading resistance and mechanical requirements fulfilment has to be verified.

2.1.1. Mechanical model.

Given the list of constraints a simplified mechanical model of instrument was created and tested by FE static and modal analyses.

2.1.1.1. Constraints for mechanical design

Optical system constraint.

Data about the optical system design are not included in this work. All calculations have been done by Dr. Bellucci (optical designer of IFSI-INAF) staff and only final result about lenses material, dimensions and position was offered as a constraint for mechanical design of micro-MIMA (Fig. 2.1).

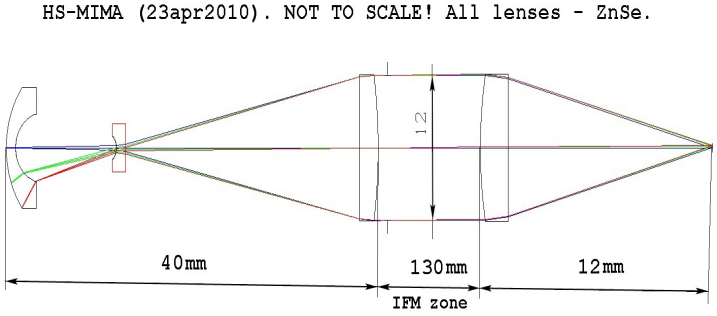

Fig. 2.1 Optical system

Rough preliminary beamsplitter dimensioning resulted in following values: minimum major (minor) semiaxis 17 (12) mm (with min thickness ratio 0.1 of max dimension).

Spectral resolution constraint

Spectral resolution is directly linked to the optical path difference provided by the instrument. That sets the geometrical constraint for the pendulum design: with the reference to Fig. 2.2. distance D between beam splitter and cubic mirror has to ensure the possible movement of the last one.

If projected spectral resolution $\Delta\sigma$ is $2cm^{-1}$, maximum optical path difference required can be computed as:
$OPD_{MAX} = 1/\Delta\sigma = 0{,}5$ cm = 5 mm.

So mirror displacement needed to provide the maximum OPD is:
MD = OPD/4 = 1,25 mm (±0,625 mm).

As the design foresees further possibility of increasing of spectral resolution up to 1 cm^{-1}, so MD should be considered as ±1,25 mm and so the gap between cubic mirrors and beam splitter (Fig. 2.2) to be kept to ensure this last MD value:
D > 1,25 mm.
Rough preliminary beamsplitter dimensioning resulted in following values: minimum major (minor) semiaxis 17 (12) mm (with min thickness ratio 0.1 of max dimension).

Spectral resolution constraint

Spectral resolution is directly linked to the optical path difference provided by the instrument. That sets the geometrical constraint for the pendulum design: with the reference to Fig. 2.2. distance D between beam splitter and cubic mirror has to ensure the possible movement of the last one.

If projected spectral resolution $\Delta\sigma$ is $2cm^{-1}$, maximum optical path difference required can be computed as:
$OPD_{MAX} = 1/\Delta\sigma = 0{,}5$ cm = 5 mm.

So mirror displacement needed to provide the maximum OPD is:
MD = OPD/4 = 1,25 mm (±0,625 mm).

As the design foresees further possibility of increasing of spectral resolution up to 1 cm^{-1}, so MD should be considered as ±1,25 mm and so the gap between cubic mirrors and beam splitter (Fig. 2.2) to be kept to ensure this last MD value:
D > 1,25 mm.

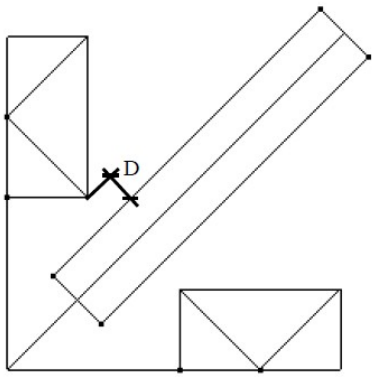

Fig. 2.2 Free distance: CCM – BS

Mass, volume, power budget constraint

Total instrument mass is 250 g, with main instrument parts of 50 g.
Instrument volume power consuming have to be decreased as possible.

2.1.1.2. Main subassemblies.

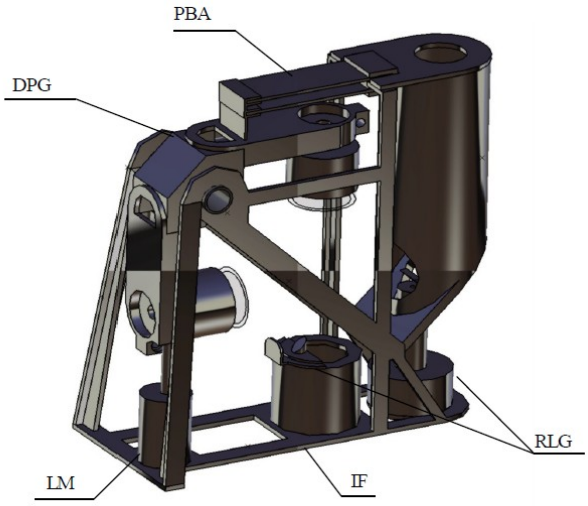

Fig. 2.3 Simplified Micro-MIMA model

To streamline the FE calculations the model has been split in a list of separately analysed subassemblies:

- instrument frame (IF);
- double pendulum group (DPG);
- piezo bender actuator assembly (PBA).

Instrument Frame (IF) (Fig 2.4) – an aluminium alloy structure - has been optimized in order to prove its sufficient stiffness characteristics for the expected excitation frequency range. For each IF analysis other elements, optical and mechanical, were modelled as concentrated masses:

- optical system of four ZnSe lenses of approximate masses (including about 30% increase for the mounting means) 1,4 g, 0,1 g, 1,2 g, 2,1 g and folding mirror of 1 g;
- beamsplitter + supports 5 g;
- actuator subassembly 2 g;
- double pendulum group13,1 g .

As locking mechanism (***LM***) and reference laser group (***RLG***) are not pointed for calculations in this work so they were included in the IF system as a schematic elements of varying masses (to guarantee the total mass constraint).

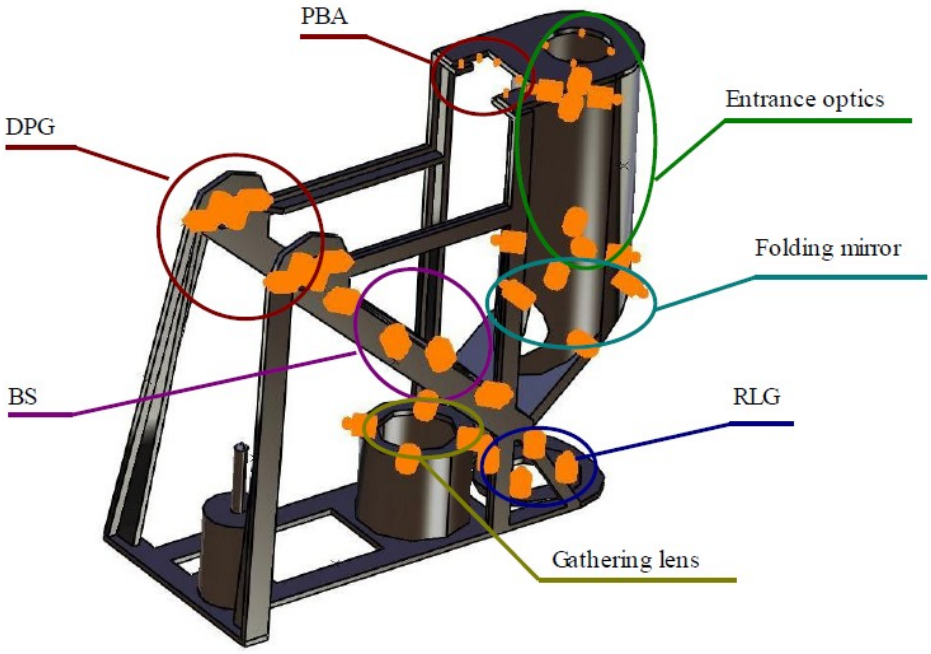

Fig 2.4 Interferometer frame with added masses

Double Pendulum Group (DPG) (Fig 2.5) is represented as two aluminium brackets on the c-flex bearing supports (material: stainless steel); to reduce system complexity those supports were substituted by simple cylindrical elements with assignment of torsional, radial and axial stiffness properties (taken from the technical data sheet of the producer [10]) of the to the mounting constraints in the model, while cubic mirrors were simplified to glass cylindrical elements with same inertial properties.

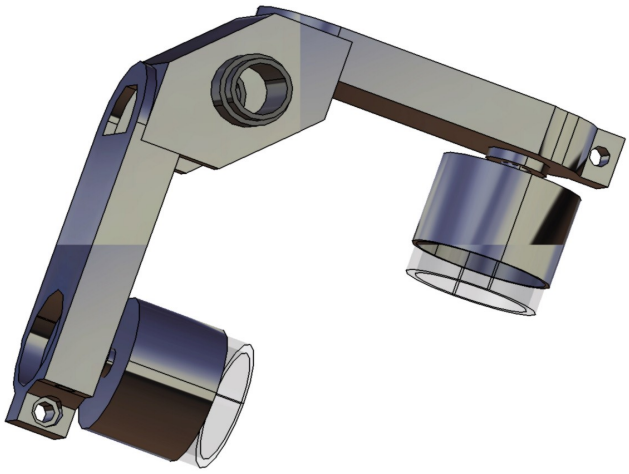

Fig 2.5 Simplified double pendulum group

Piezo Bender Actuator (PBA) subassembly (Fig 2.6) consists of 2 piezo bender actuators, between the clamp element and the contact element (joints piezo actuators to the pendulum bracket). This structure doesn't undergo specific analysis as technical data for actuators is provided by the producer [11] and answer the requirements, while mounting is represented in just a schematic way.

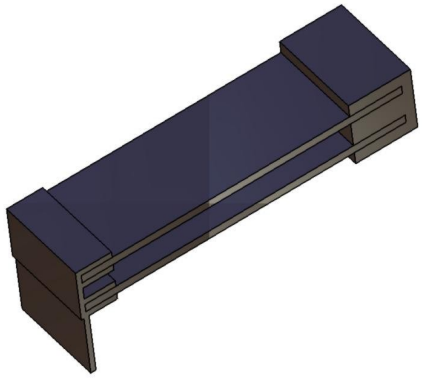

Fig 2.6 Piezo bender actuators subassembly

Finally all model components are brought together in the following Table 2.1.

Subassembly	Element	Mass, [g]	Total mass, [g]
Optical system			
Lenses	Entrance optical system + mounting	2,7	
	Positive gathering lens + mounting	1,9	
	RLG detector subgroup	0,2	
			4,8
Beamsplitter	Beamsplitter + mounting	5	5
Cubic mirrors	Cubic corner mirror	2 x 1	2
	Mirror holder	2 x 1,6	3,8
			5,8
Folding mirror	Folding mirror + mounting	1	1
		Optical system total mass	**16,6**
Mechanical system			
IF	Frame	17	
	Top cover	0,9	
			17,9
DPG	Brackets	2 x 2,5	5
	C-flex bearings	2 x 0,15	0,3
	DPG base	2	
			7,3
PBA	Actuator	2 x 0,5	1
	Clamp element	0,7	
	Contact element	0,3	
			2
		Mechanical system total mass	**25,2**
Additional components			
Mass budget for small details	LM, RLG, other additional elements		customized

Table 2.1 Model components

2.1.1.3. FE-models.

The list of materials and their mechanical properties used in micro-MIMA is presented in the following Table 2.2.

	Young modulus, [MPa]	Poisson ratio	Density, [kg/m^3]	Tensile strength , [MPa]	Yield strength, [MPa]
Al alloy 7075-T6	7*10^4	0,35	2710	530	475
Stainless steel	19,3*10^4	0,27	7990	800	600
KBr	2,7*10^4	0,203	2753	3,3	n.a.
ZnSe	6,72*10^4	0,28	5270	55,1	n.a.
Glass	6,5* 10^4	0,161	2190	n.a.	n.a.

Table 2.2 Material properties

IF subassembly.

To get the iso-static structure following restraints were applied on the model (Fig. 2.7):

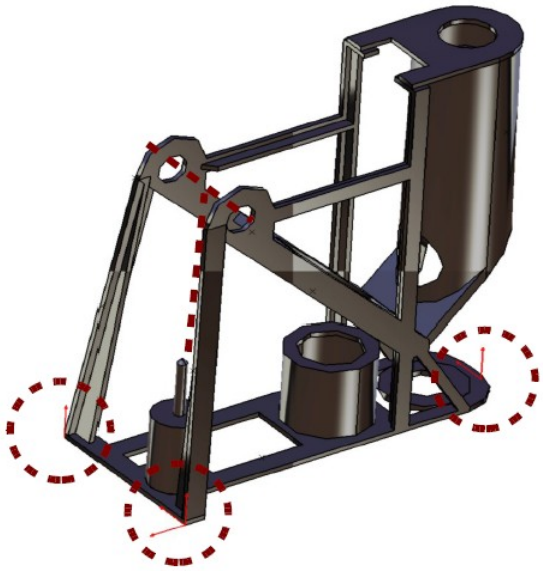

Fig. 2.7 IF assembly

Besides inertia properties assignments presence of the DPG structure is also indicated by rigid connection property between mounting surface for bearings and locking mechanism.

To achieve reliable results was created a parabolic tetrahedron elements mesh with element size of 0,5 mm, value identified as the minimum to have at least 2 elements per thickness (Fig. 2.8), what Catia recognizes as adequate mesh quality index).

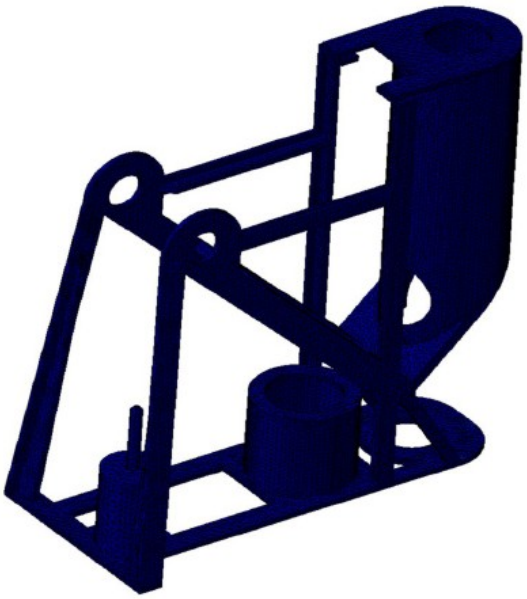

Fig. 2.8 IF mesh

DPG subassembly.

This structure is fixed on the frame by using bearings support and rotation around the pendulum axis is prevented by locking mechanism support (Fig. 2.9).

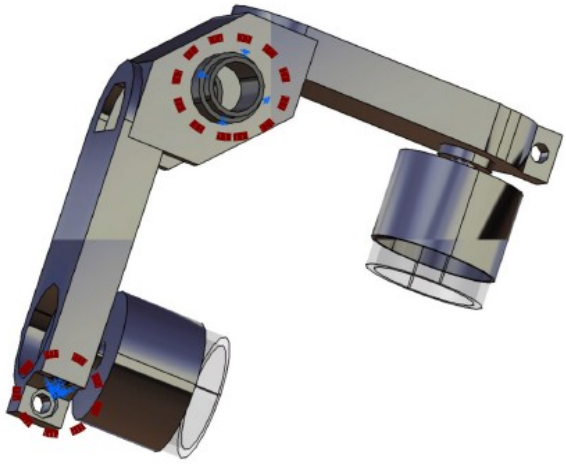

Fig. 2.9 DPG assembly

Contact between pendulum base and bearings is described using stiffness properties from the c-flex technical data:
radial stiffness – 350 N/mm;
axial stiffness – 580 N/mm;
rotational stiffness – 0,01 Nm/rad.

For mesh were also chosen parabolic tetrahedron elements of 0,5 mm size (Fig. 2.10), found to be an acceptable trade off between results accuracy and computation time.

Fig. 2.10 DPG mesh

2.1.2. Static stress analysis

Static stress analyses were performed on the described structures for the equivalent acceleration of 1000 m/s2 along X, Y, Z directions.
For each loading condition should be fulfilled the following inequality:

$$SM = \frac{\sigma_{yield}}{\sigma_{max} \cdot SC} > 1 \quad (1)$$

where σ_{yield} is the yield stress, σ_{max} is the max Von Mises stress and SC is the safety coefficient.

IF subassembly

Results from the static stress analyses on the IF structure are presented below (Fig. 2.11):

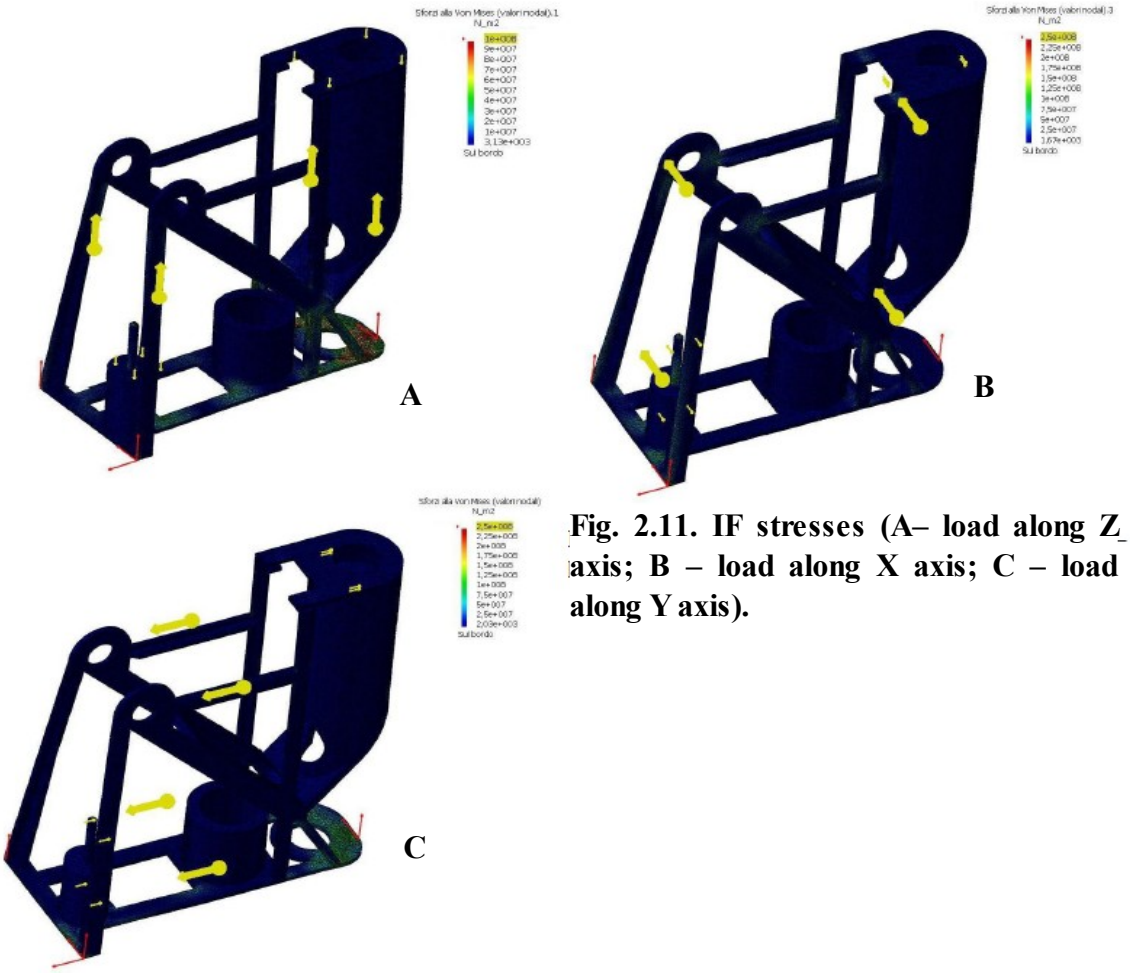

Fig. 2.11. IF stresses (A– load along Z axis; B – load along X axis; C – load along Y axis).

Having the aluminium alloy structure

σ_{yield} = 475 MPa

and being the maximum Von Mises stresses along each direction

σ_{max} X = 125 MPa,

σ_{max} Y = 75 MPa,

σ_{max} Z = 100 MPa,

with safety coefficients

SC_X = 1,5,

SC_Y = 1,5,

SC_Z = 2

safety margins are

SM_X = 2,5,

SM_Y = 4,2,

$SM_Z = 2,4$.

It has to be noticed the inequality (1) is accomplished for all 3 loading cases.

DPG subassembly

Results from the static stress analysis on the DPG structure are presented below (Fig. 2.12):

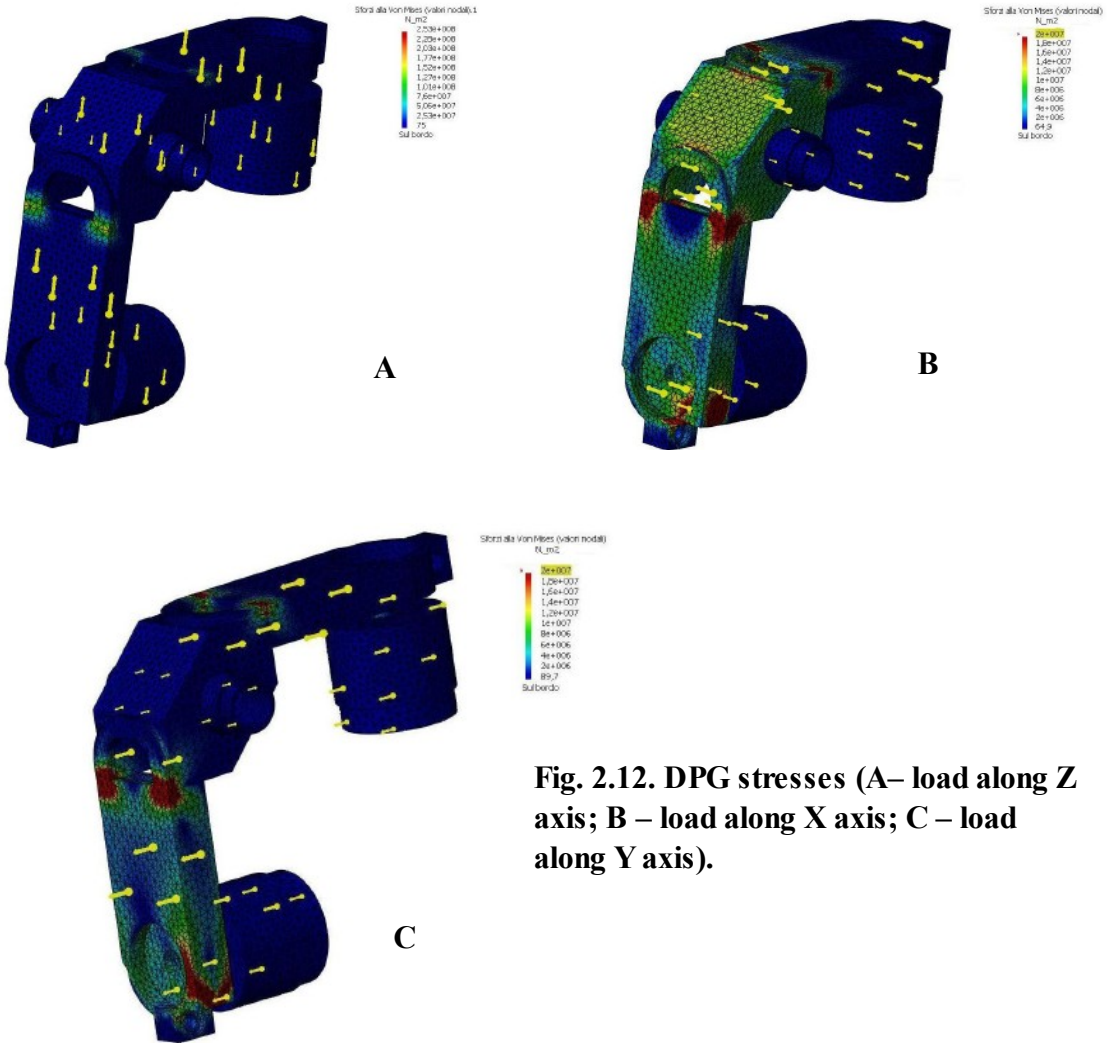

Fig. 2.12. DPG stresses (A– load along Z axis; B – load along X axis; C – load along Y axis).

Having the aluminium alloy structure

σ_{yield} = 475 MPa

and being the maximum Von Mises stresses along each direction

σ_{max} X = 20 MPa,

σ_{max} Y = 20 MPa,

σ_{max} Z = 150 MPa,

with safety coefficients

SC_X = 1,5,

SC_Y = 1,5,

SC_Z = 2

safety margins are

SM_X = 15,8,

SM_Y = 15,8,

SM_Z = 1,6.

It has to be noticed the inequality (1) is accomplished for all 3 loading cases.

2.1.3. Frequency analysis.

Modal analyses have been performed to assure that all the structure natural frequencies are above 150 Hz limit.

IF subassembly

The first five natural frequencies are listed in the Table 2.3.

Mode	1	2	3	4	5
Frequency, [Hz]	245	253	398	561	960

Table 2.3. IF: natural frequencies

First two vibration modes are shown on the Fig. 2.13. First one (245 Hz) consists of base plane bending; second one (253 Hz) – in optical entrance group rotation around the base.

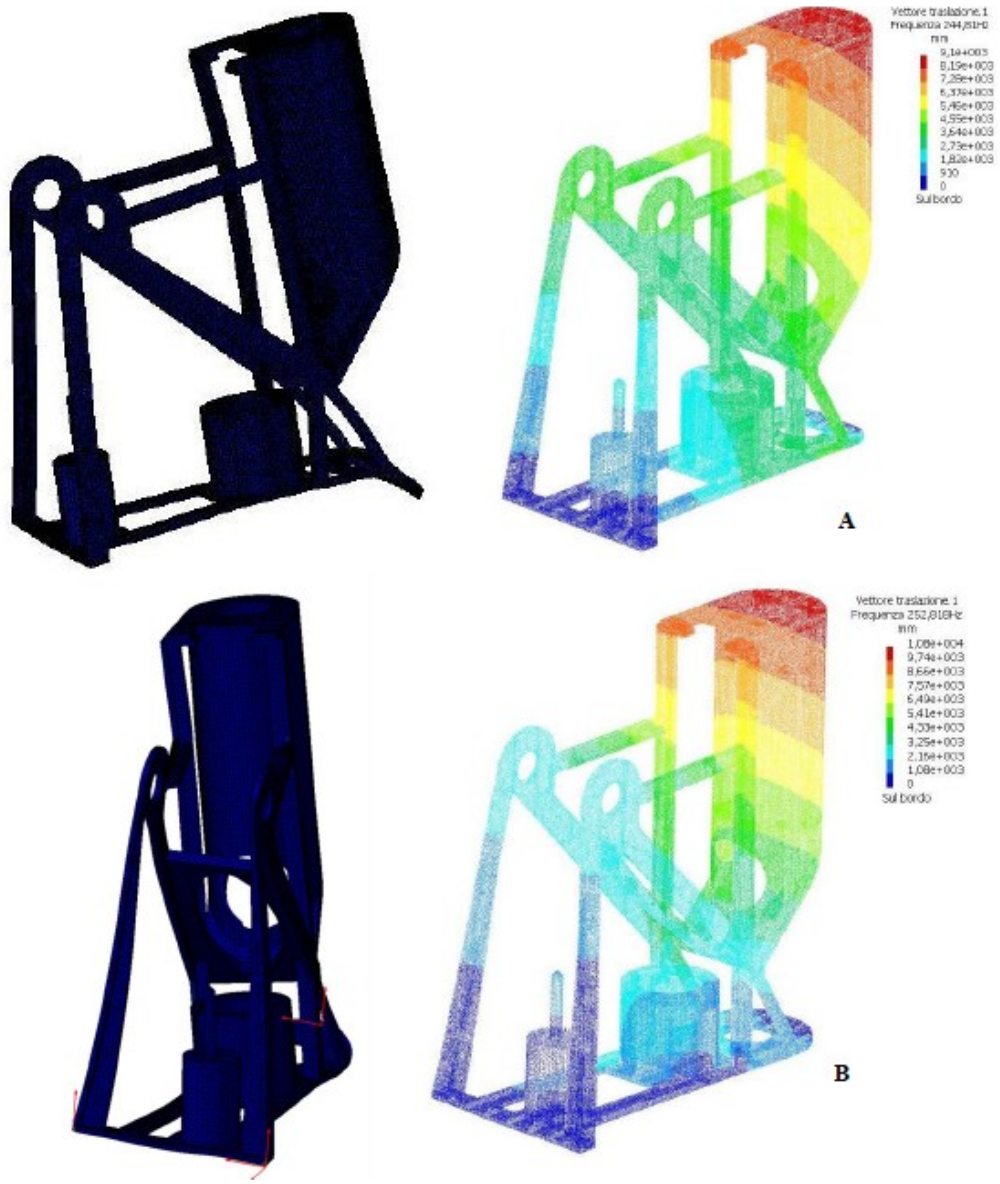

Fig. 2.13 IF vibration modes (A – 245 Hz; B – 253 Hz)

DPG subassembly.

The first five DPG natural frequencies calculated are listed in the Table 2.4.

Mode	1	2	3	4	5
Frequency, [Hz]	403	543	1175	2372	2561

Table 2.4. DPG natural frequencies

First vibration mode is shown on the Fig. 2.14.

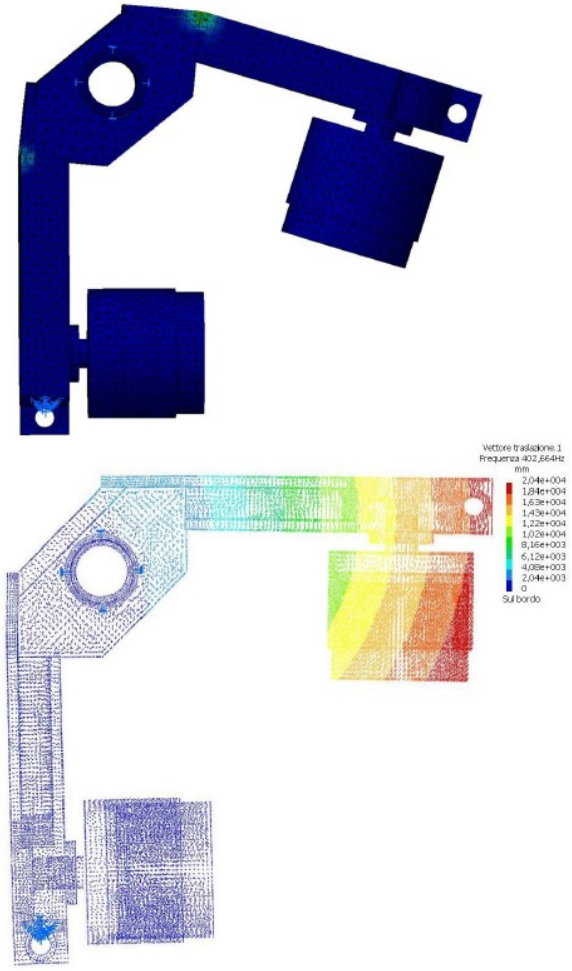

Fig. 2.14. DPG vibration mode (403 Hz)

2.1.4. Certain components calculations

In this paragraph will be summarized requirements for the locking mechanism and performed choice of such standard elements as C-flex bearings and piezo actuators.

2.1.4.1. Requirements for the locking mechanism

According to the loading conditions following requirements for the locking mechanism are calculated (Fig. 2.15):

- min pin diameter d, mm;
- locking force F_{lock}, N;

- minimum contact length a, mm.

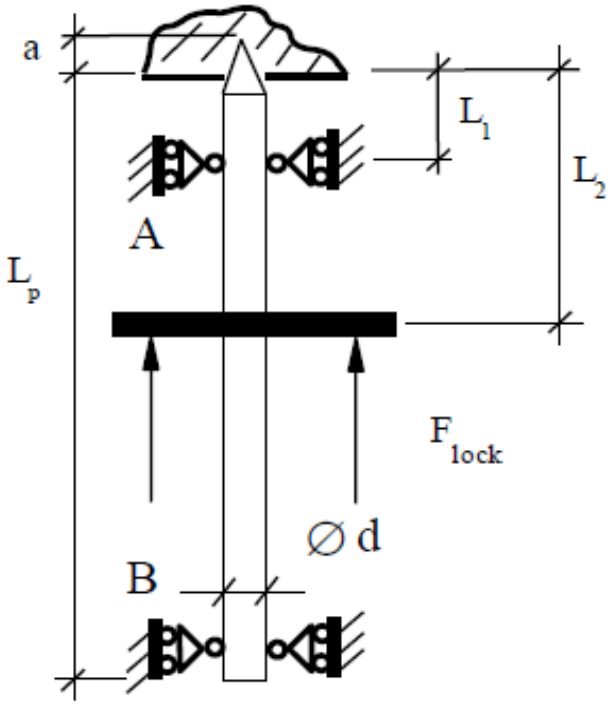

Fig. 2.15 Schematic representation of locking mechanism

All requirements are presented for the worst case of loading condition when acceleration on the DPG is directed as it is shown on the Fig. 2.16.

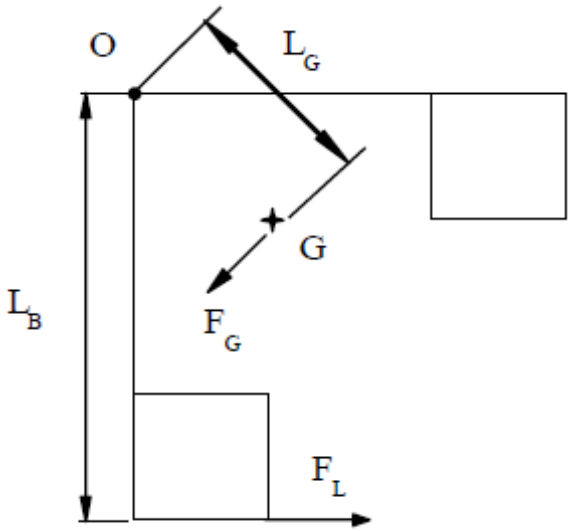

Fig. 2.16. DPG loading case

$F_G = 1000*MASS_{DPG} = 13$ N;
$L_B = 37$ mm;
$L_G = 12$ mm;
$L_p = 26{,}5$ mm;
$L_1 = 10$ mm;
$L_2 = 13$ mm.

$\sum M_O = 0 \Rightarrow F_L = F_G*L_G / L_B = 4{,}2$ N.

Locking force F_{lock}

For ideal line contact between two cones (Fig. 2.17 A) we have $F_{lock} > F_{axial} = F_L*tg\alpha$.

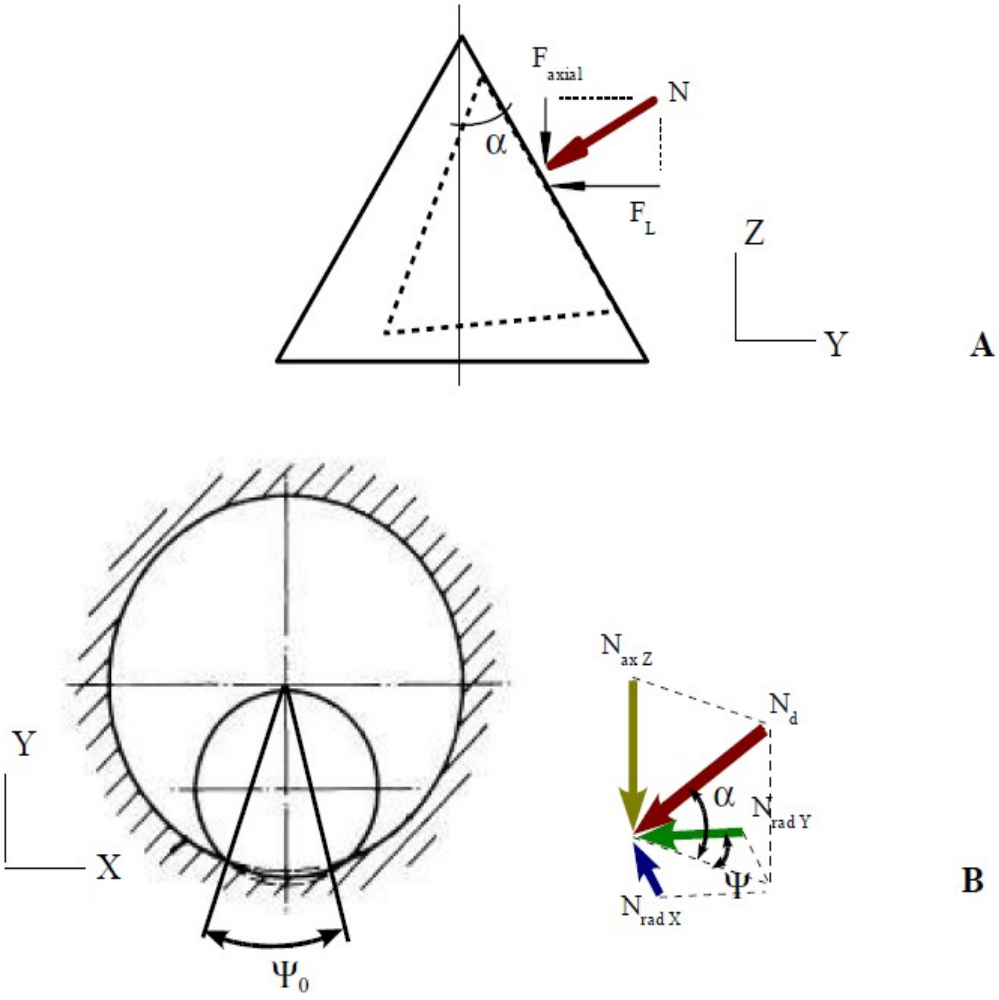

Fig. 2.17 Cone contact (A – ideal line contact; B – real surface contact)

Real contact is not a line but a surface one (Fig. 2.17 B), in that case total normal force in contact can be obtained from integration:

$$N = \int_{S_{contact}} N_d \, dS \quad .$$

Having $N_{rad\ X}$, $N_{rad\ Y}$ and $N_{ax\ Z}$ – projections of N_d (Fig. 2.17 B) we can write following expressions:

$$\int_{S_{contact}} N_{ax} \, dS = F_{axial} \quad ,$$

$$\int_{S_{contact}} N_{rad\,X} \, dS = F_L \quad ,$$

$$\int_{S_{contact}} N_{rad\,X} \, dS = 0 \quad .$$

As

$$dS = R \, d\psi \, dL \quad ,$$

$$N_{rad\ X} = N_d \cos\alpha \cos\psi \quad ,$$

$$N_{ax\,Z} = N_d \sin\alpha \quad ,$$

we can rewrite

$$F_L = 2 \int_{\Psi_0/2} \int_{L} N_d \cos\alpha \cos\psi \, d\psi \, R \, dL \quad ,$$

$$F_{axial} = \int_{\Psi_0} \int_{L} N_d \sin\alpha \, d\psi \, R \, dL \quad .$$

So we obtain

$$F_{axial} = F_L \tan\alpha \frac{\Psi_0/2}{\sin(\Psi_0/2)} \quad ,$$

where Ψ_0 is the contact angle; generally it depends on cone angles of contacting surfaces and $\Psi_{0\,MAX} = \pi$. This is the worst case that can be used to determine the required locking load.

So $F_{lock} > \pi/2 * F_L * \tan\alpha$.

It should be noticed that to account to the friction the above angle α is not the purely geometric angle but includes the friction angle i.e. if θ is the cone half angle and is φ friction angle, so:

$\alpha = \theta - \varphi$.

For different cone angle α we get different F_{lock} (Annex A.1). Results are presented in Table 2.5.

Pin diameter

Pin loading conditions are presented on Fig. 2.18.

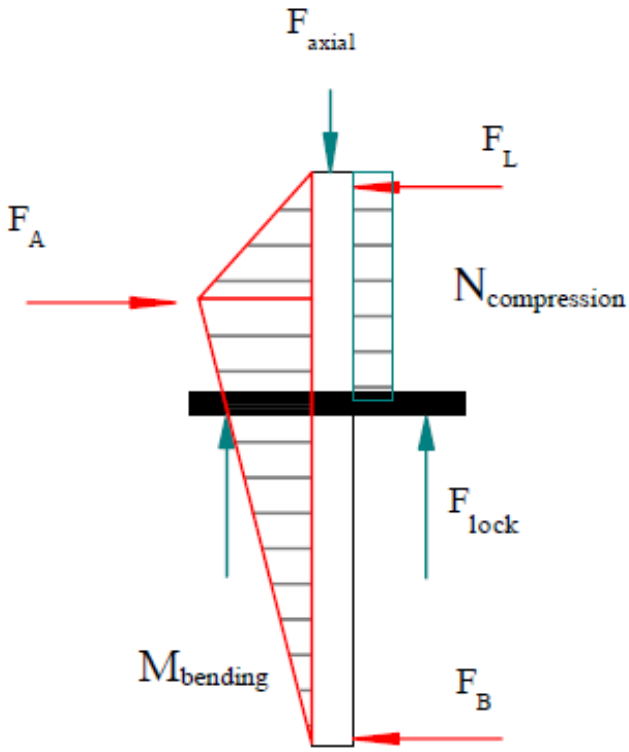

Fig. 2.18 Pin internal actions diagram

$\sigma_{max} = \sigma_{bending\ max} + \sigma_{compression} \leq \sigma_{yield}$ /SC;

where safety coefficient SC = 2,
yield stress σ_{yield} = 475 MPa.

$\sigma_{bending\ max} = M_{bending\ MAX}/W = F_L * L_1/ W$;
$\sigma_{compression} = N_{compression}/A = F_{axial}/ (\pi * d_{min}^2/4)$;
$W = \pi * d_{min}^3/32$.

Constraint will be:
$\varnothing d \geq d_{min}$.

For different cone angle α we get different $\varnothing d$ (Annex A.1).
Results are presented in Table 2.5.

Contact length

Min contact length required might be calculated from the hertzian contact pressure.
To simplify the calculations we reduce the cone-cone contact to cylinder-cylinder one (Fig. 2.19) with cylinder length L equal to cone generatrix and radii R_1 (outer cylinder) and R_2 (inner cylinder) – radii of cones at the mid-surface plane.

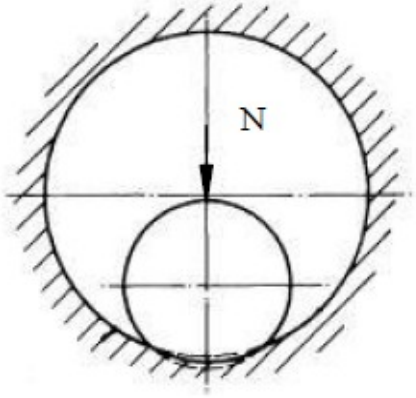

Fig. 2.19 Simplified pin-hole contact representation

$R=\frac{a}{\sqrt{2}}*\tan\alpha$ – due to the fact that cone surface is halved at $\frac{a}{\sqrt{2}}$ height:
$S_{cone\ area}=\pi RL$,
where R – radius of base circle and L – the generatix;
$R=a*\tan\alpha, L=\frac{a}{\cos\alpha} \Rightarrow S_{cone\ area} \sim a^2 \Rightarrow S^{half}_{cone\ area}=S_{cone\ area}/2$ at
$a^{half}=\frac{a}{\sqrt{2}}$.

Considering that cone angles α_1, α_2 slightly different (e.g. 5 % difference) we get
$R_{1(2)}=\frac{a}{\sqrt{2}}*\tan\alpha_{1(2)}$,
$\alpha_1=\alpha, \alpha_2=0{,}95*\alpha$.

In that case maximum pressure is equal to:
$p_{max}=\sqrt{\frac{E_S*N}{\pi*R*L}}$,
where

$\frac{1}{E_S} = \frac{1-\nu_1^2}{E_1} + \frac{1-\nu_2^2}{E_2}$ (E_1,E_2 are the elastic moduli and ν_1,ν_2 the Poisson's ratios associated with each body; considering pin material aluminium alloy as well we get $E_1 = E_2$);

$N = F_{axial} / \sin\alpha$;

$\frac{1}{R} = \frac{1}{R_2} - \frac{1}{R_1}$ (R – effective radius).

To avoid adhesion the following inequality has to be fulfilled:

$p_{max} \le \sigma_{yield} / SC$, where SC – safety coefficient; SC = 3 in case of adhesion calculations [4].

Using those equations for different cone angle α we get different a (Annex A.1). Results are presented in Table 2.5.

Cone angle α, °	Locking force F_{lock}, N	Pin diameter d, mm	Contact length a, mm
30	3.8	1,3	0.24
45	6.6	1,4	0.18
60	11.4	1,6	0.17

Table 2.5 Locking mechanism parameters

2.1.4.2 C-flex bearings choice.

For micro-MIMA we use single-end cross-flexure bearings (C-Flex Bearing Co., Inc) represented on Fig 2.20.

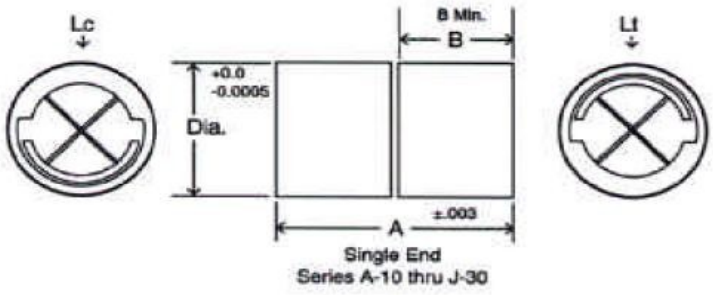

Fig 2.20 Cross-flexure single end bearings

Main size and performance properties of those products are shown in Table 2.6.

Series	Dia, mm	Spring rate, Nmm/°	A, mm	B, mm	Lr, N	La, N	Θ_{MAX}, °
A10	3,18	0.0339	5.08	2.24	4,23	27,05	±15
A20		0.2034			39,59	56,49	±7,5
A30		1.6722			112,54	112,54	±3,7
B10	3,97	0.0452	6.35	2.9	6,23	39,86	±15
B20		0.418			60,94	87,18	±7,5
B30		3.3443			174,81	112,54	±3,7
C10	4.76	0.0791	7.62	3.45	8,9	55,51	±15
C20		0.6779			86,74	124,1	±7,5
C30		5.4458			248,21	248,21	±3,7
D10	6.35	0.2034	10.16	4.67	16,9	101,06	±15
D20		1.6722			155,69	22,41	±7,5
D30		13.3886			444,82	444,82	±3,7

Lr – radial load capacity, min of Lc (compression) and Lt (tension); La – axial load capacity.

Table 2.6 C-flex bearings list

On DPG there are acting 2 main forces: from locking mechanism (directed always radially to bearings) and inertial force oriented inversely to acceleration and thus might be directed variously).
Total load on bearings is vectorial sum of those two forces.
$\mathbf{F}_B = \mathbf{F}_G + \mathbf{F}_{lock}$

So maximum possible radial force on each bearing would be:

$F_{B\ RAD\ MAX} = F_G + F_{lock\ max} = 24$ N;
$F_{B\ AXIAL\ MAX} = F_G = 13$ N.

Choice then should be made by min spring rate bearing (so min actuator force and thus power consumption necessary) with enough load capacity.

That would be A20.

2.1.4.3. Number and position of piezo actuators.

For micro-MIMA we use PICMA Bender actuators (Fig. 2.21).

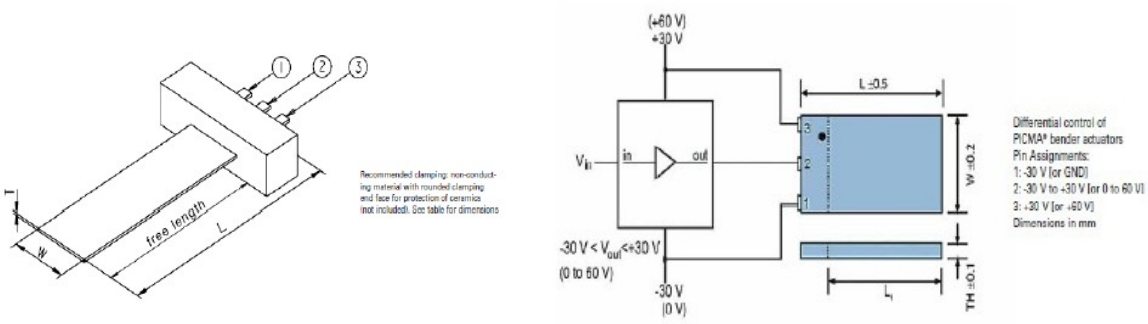

Fig. 2.21 Piezo bender actuator

Technical data for those products is presented in Table 2.7.

Order number	Nominal displacement, μm	Dimentions, LxWxT, mm	Blocking force, N	Resonant frequency, Hz
PL112.10	±80	17,8 x 9,6 x 0,65	±2,0	>1000
PL122.10	±250	25,0 x 9,6 x 0,65	±1,1	660
PL127.10	±450	31,0 x 9,6 x 0,65	±1	380
PL128.10	±450	35,5 x 6,3 x 0,75	±0,5	360
PL140.10	±1000	45,0 x 11,0 x 0,6	±0,5	160

Table 2.7. Piezo actuators technical data

For actuator choice we consider displacement and force requirements (Fig 2.22).

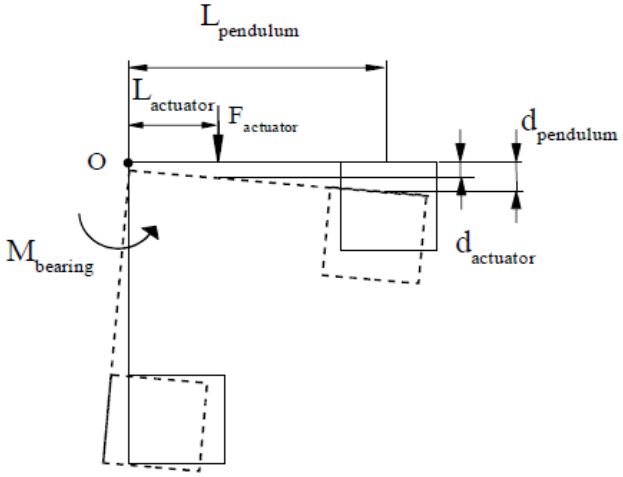

Fig. 2.22. Actuator action scheme

$$d_{actuator} = d_{pendulum} * L_{actuator} / L_{pendulum} \quad ,$$

where $d_{pendulum} = \pm 1{,}25$ mm,
$L_{pendulum} = 28{,}5$ mm.

$$F_{actuator} = \frac{M_{bearing} + \Delta M_{gravity}}{L_{actuator}} = \theta * k / L_{actuator} + \Delta M_{gravity} / L_{actuator} \quad \text{(Annex A.2)},$$

where is Θ – rotation angle, $\tan\theta = d_{pendulum} / L_{pendulum} \Rightarrow \Theta = 2{,}5°$;
k – spring rate, $k = 2 * K_{bearing} = 0{,}4$ Nmm/°.

For PL127.10 optimal positioning will be $L_{actuator} = 5{,}13$ mm (Annex A.2).

Taking $L_{actuator} = 5$ mm we obtain the following:

$F_{actuator} = 0{,}33$ N,
$d_{actuator} = d_{pendulum} * L_{actuator} / L_{pendulum} = 0{,}23$ mm.

$$F_{actuator\,available} = F_{blocking} * (1 - d_{actuator} / d_{nominal}) = 0{,}48 \quad \text{N}.$$

Minimum number of actuators

$$N = integer\left(\frac{F_{actuator}}{F_{actuator\ available}} SC\right) = integer\,(0{,}825) = 1 \quad ,$$

where SC – safety coefficient for elastic force, SC = 1,2 [4].

To relieve the actuator operating conditions in model was chosen number of actuators N = 2.

For mock up choosing PL127.10 actuator and applying it at 1/3 of pendulum arm (choice is based on geometrical dimensions of the model) we get:

$L_{actuator} = L_{pendulum}/3 = 9{,}5$ mm;
$d_{actuator} = d_{pendulum}/3 = 0{,}42$ mm;
$F_{actuator} = 0{,}11$ N (*Note: as in mock-up pendulum group will rotate in horizontal plane, we do not have moment created by gravity force*).

$$F_{actuator\,available} = F_{blocking} * (1 - d_{actuator} / d_{nominal}) = 0{,}07 \quad \text{N}.$$

So number of actuators
$N = \text{integer}(F_{actuator}/F_{actuator\ available}) = 2$.

2.1.5. Conclusions.

Performed analyses show that simplified scheme of the micro-MIMA can resist predicted mechanical loads on the structures. Thus feasibility of the proposed model structure is proved with mass requirement fulfilment. Performed analysis permits to make preliminary decision about choice and parameters of such elements like bearings, actuators, locking system to be further used on the detailed structure of the micro-MIMA.

2.2. Thermal design.

There are different simulated scenarios of Martian environment which provide the temperature field on the instrument. Thermoelastic analysis was performed in order to find temperature distribution on the structure during the worst scenario and evaluate optical misalignment that it creates.

2.2.1. Thermal model.

2.2.1.1. Structure for thermal analysis.

For thermoelastic analysis main interest is related to those structural elements that hold optical subsystem. Thus in instrument thermal model the 2 main subassemblies from the mechanical one are used (IF and DPG), while other elements are represented as additional inertia properties (Fig. 2.23).

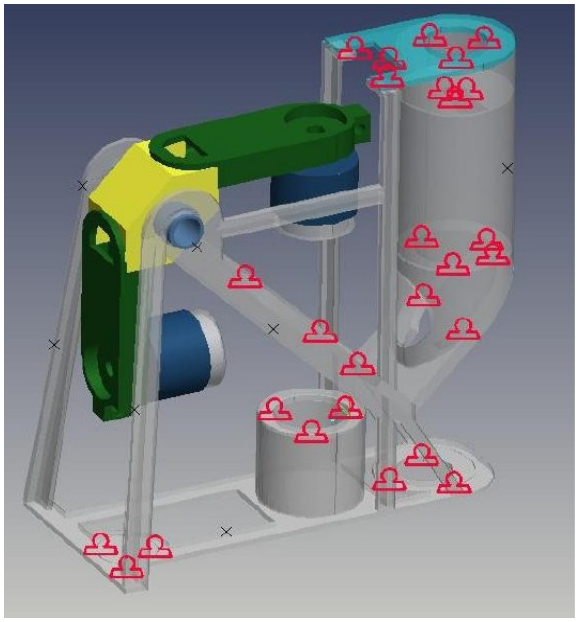

Fig.2.23. Model for thermal analysis.

Model was constrained same way as for mechanical analysis providing an iso-structure (Fig.2.24).

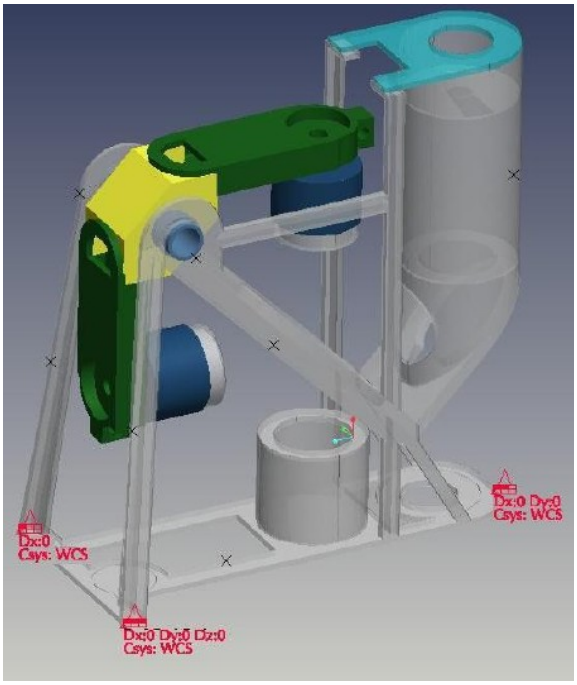

Fig.2.24 Mechanical constraints

2.2.1.2. Material properties.

Thermal properties for micro-MIMA materials are presented in Table 2.8.

Material	Thermal expansion, m/m°C	Thermal Conductivity, N/s°C
Al alloy 7075-T6	$2{,}36*10^{-5}$	172
Stainless steel	$1{,}17*10^{-5}$	16,2
Glass	$7*10^{-5}$	4,82

Table 2.8. Material thermoelastic properties

2.2.1.3. Simplified thermal model

From the worst predicted Mars scenario – dust storm (Fig. 2.25) – using ESATAN-TMS software (ESA/Alsthom property) were extracted temperatures at the characteristic points of micro-MIMA main outer surfaces.

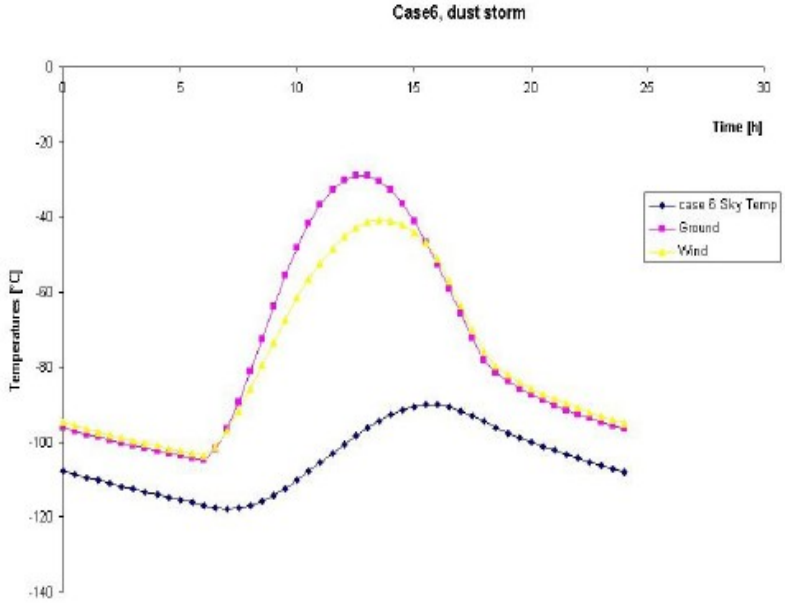

Fig. 2.25 Mars environment scenario: dust storm

From above data was created the temperature load on the instrument model (Fig. 2.26).

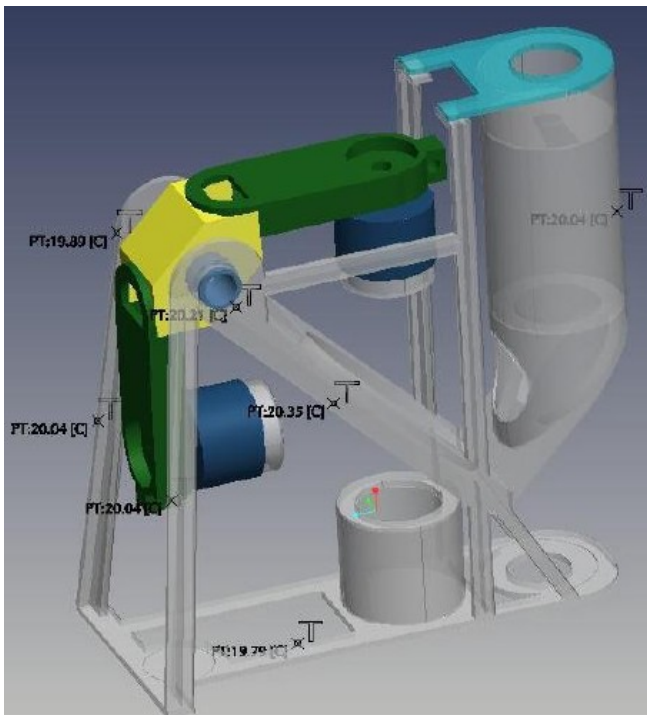

Fig. 2.26 Prescribed temperatures

2.2.2. Thermoelastic analysis.

Using Pro-Engineer software a temperature distribution on the structure under predicted temperature load (Fig. 2.27) was calculated.

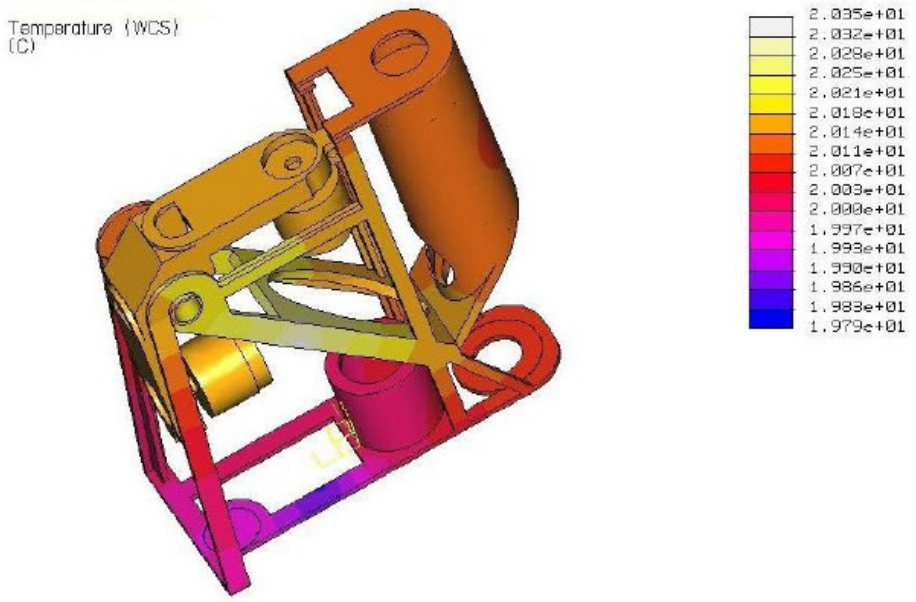

Fig. 2.27 Temperature distribution

Another obtained result is the displacement field of elements (Fig. 2.28).

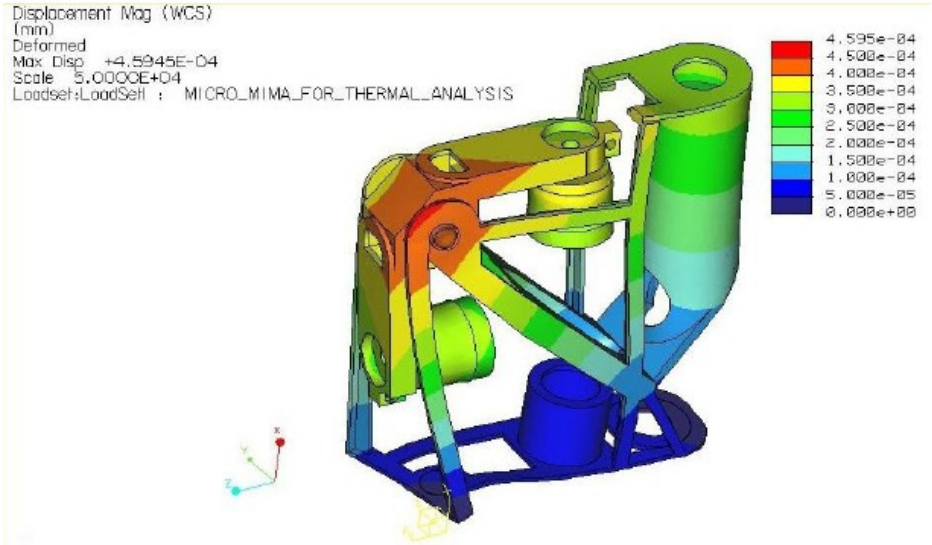

Fig. 2.28 Thermoelastic analysis: displacement field

Also thermoelastic analysis provides stress field on the structure (Fig 2.29).

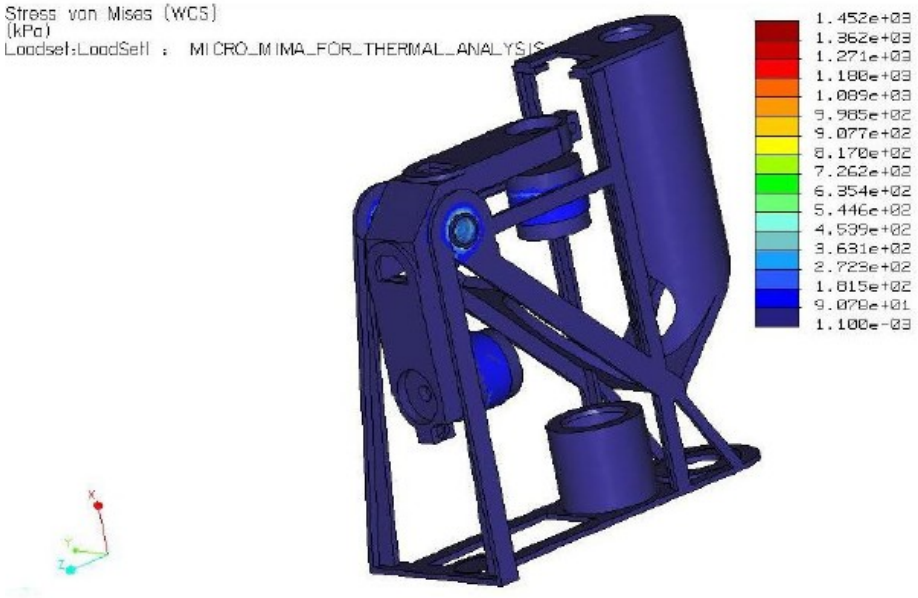

Fig 2.29 Thermoelastic analysis: stress field

As it is seen from the Fig. 2.29 some stresses appear in the area of contact between elements with different thermal expansion coefficients. However above levels of stresses are not consistent with real situation as in the analysed model all contacting elements were represented in a schematic way.

2.2.3. Optical elements misalignments calculation

Optical elements misalignments must not exceed some levels in order to ensure instrument efficiency. Those levels provide limit values for optical element shifts:

- displacements max 0,5 μm;
- tilt max 1 arc sec.

From the displacement field on the structure were picked up data about optics mounting surfaces shifts (see Annex B). Those shifts describe 3-dimensional movement of optical elements and cause instrument misalignments. Data about those shifts is provided in Table 2.9.

Optical element		Displacement in vertical direction, μm	Displacement in horizontal plane, μm		Tilt, arc sec
		X	Y	Z	
Entrance optics	Lens 1	0,243	0,103	0,184	0.0003
	Lens 2	0,222	0,091	0,167	0.0004
	Lens 3	0,148	0,051	0,105	0.0020
Gathering lens		0,002	0,003	0,075	0.0031
Folding mirror		-	-	-	0.187
Beamsplitter		-	-	-	0.092
CCM	CCM1	0,215	-	0,255	-
	CCM2	0,042	-	0,310	-
CCM relative displacement		0,174		0,055	

Table 2.9 Optical system misalignments

As it is seen from the results there is no shift of any optical element which could provide some critical misalignment in optical system.

3.4. Conclusions

Performed thermoelastic analysis ensures instrument reliable efficiency under the worst Martian environment scenario. At the same time further thermal stress analysis should be performed on the more detailed structure with exact representation of optical elements mounting.

Chapter 3.

Design of laboratory mock up.

This chapter is devoted to the laboratory mock up design for micro-MIMA performance characteristics check. It will be derived from the previously created simplified mechanical model of instrument. Being generally simplified from the structural point of view this mock up will include detailed representation of the main elements mounting, regulation and positioning.

3.1. Optical elements mounting.

To the mock up optical elements belong:

- beamsplitter;
- cubic corner reflectors;
- entrance optics group;
- gathering lens;
- photodetector;
- reference laser group (design left for customized solution).

3.1.1. Beamsplitter group.

Beamsplitter is inserted in the cylindrical part (Fig. 3.1) mounted on the beamsplitter frame element. To this part it is connected by glue injected through two tiny slots. To guarantee exact position of the beamsplitter group middle optical plane a compensator (element totally identical to beamsplitter) is inserted in beamsplitter frame from another side (using the same mounting scheme).

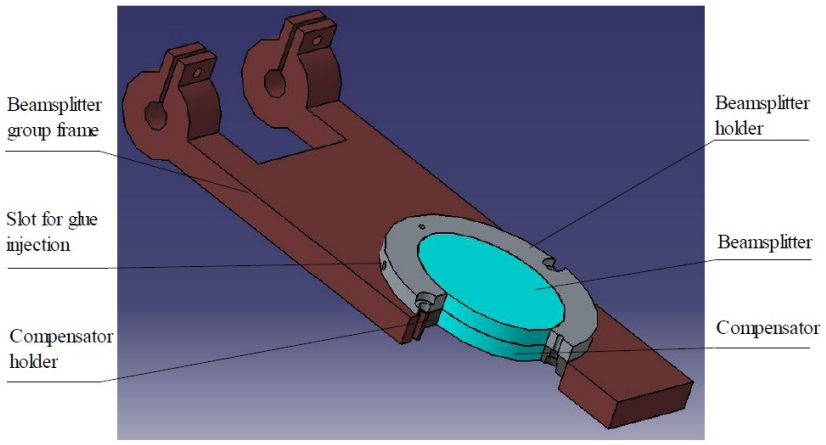

Fig. 3.1 Beamsplitter group mounting

Such solution provides good accuracy for the instrument performance check, while would be inconsistent for any kind of load tests, because glue connection is very delicate.

3.1.2. Cubic corner reflectors

Cubic corner reflectors of required dimensions are chosen from the producer company catalog [9]. Their mounting on the double pendulum group brackets has to provide the possibility of regulation of axis direction for further alignment. Solution method is represented on the Fig.3.2, where regulation requirements are fulfilled by usage of a spherical joint.

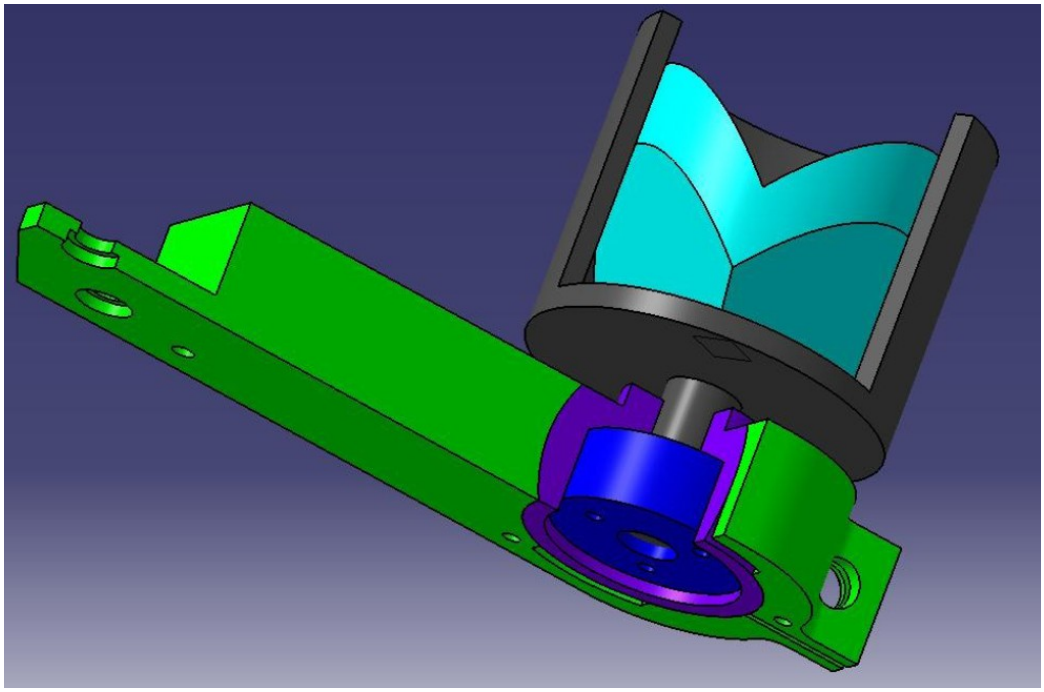

Fig.3.2 CCM mounting scheme

For regulation bracket arm and CCM group are connected to two separate cylinders as it is shown in the scheme on Fig. 3.3. Axis adjustment is performed by two radial screws.

After regulation is done spherical joint is strengthened by tightening the fixing screw on the bracket arm.

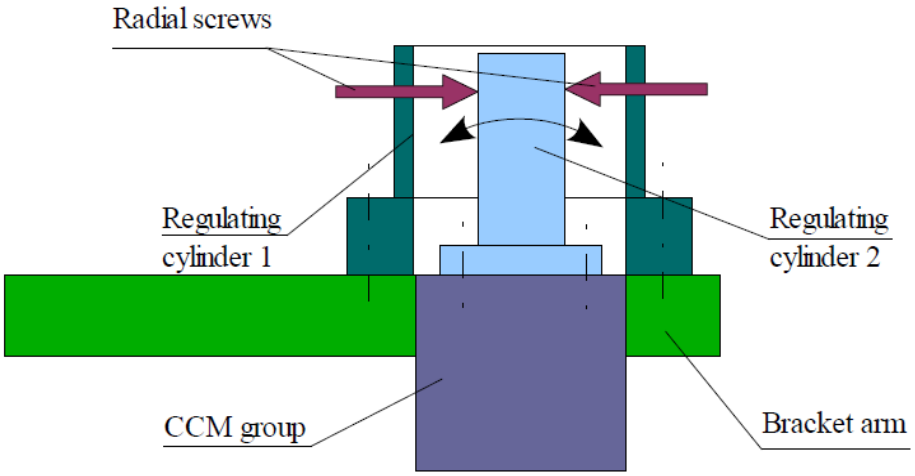

Fig. 3.3 CCM regulation scheme

3.1.3. Entrance optics system plus gathering lens

mounting of all lenses follows basically same approach: lens in inserted in the frame (replicating its surface) and from another side is jammed be a threaded pin (Fig.3.4). To protect lens from stresses an elastic separator is used between lens and pin.

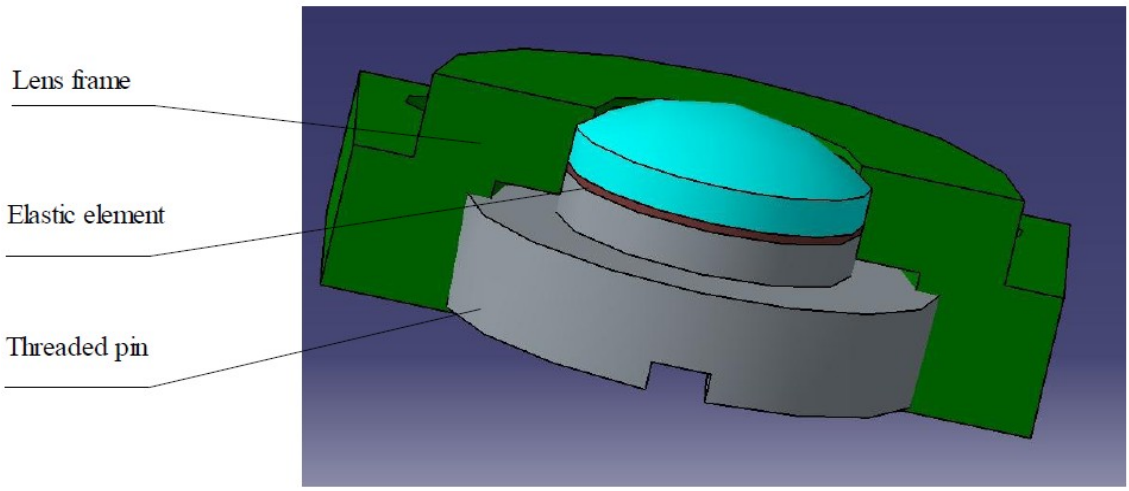

Fig. 3.4 Entrance lens mounting scheme

On Fig. 3.5 general views for other lenses' mounting is presented.

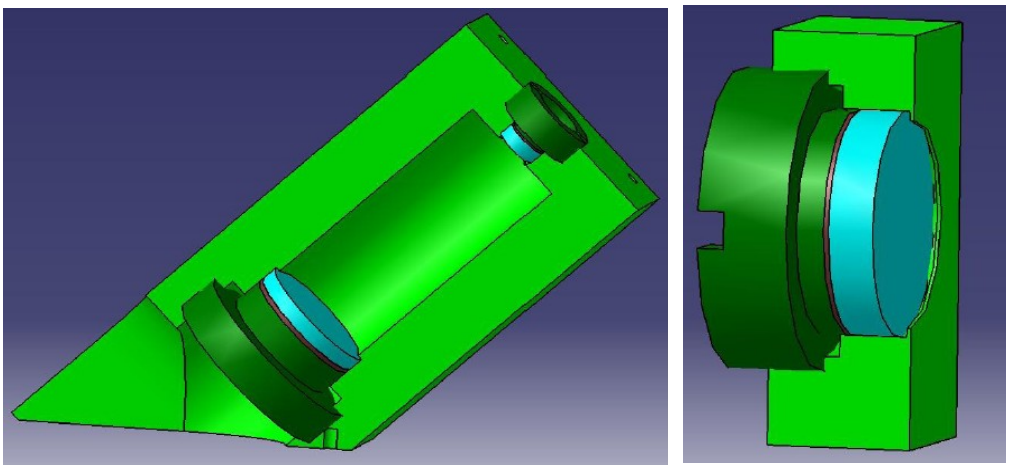

Fig. 3.5 Lenses mounting in the model

Folding mirror is glued in the slot on the bottom cover of optical entrance cylinder (Fig. 3.6).

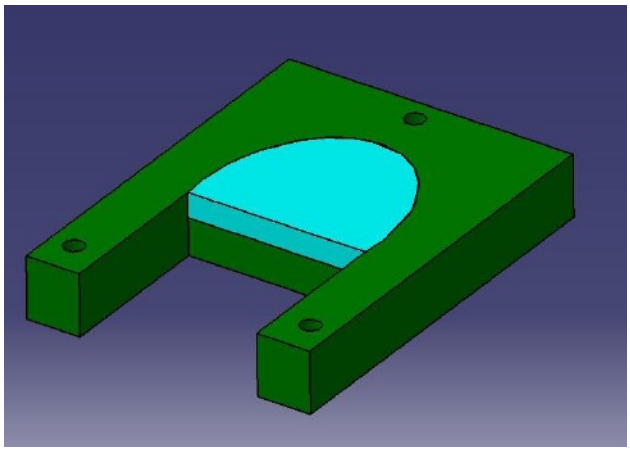

Fig. 3.6 Folding mirror mounting

Rectangular opening in the folding mirror group is left for the customized solution for reference laser group.

3.1.4. Photodetector.

Photodetector and its characteristics are taken from the producer company data sheet [12]. Its mounting is represented on the Fig. 3.7.

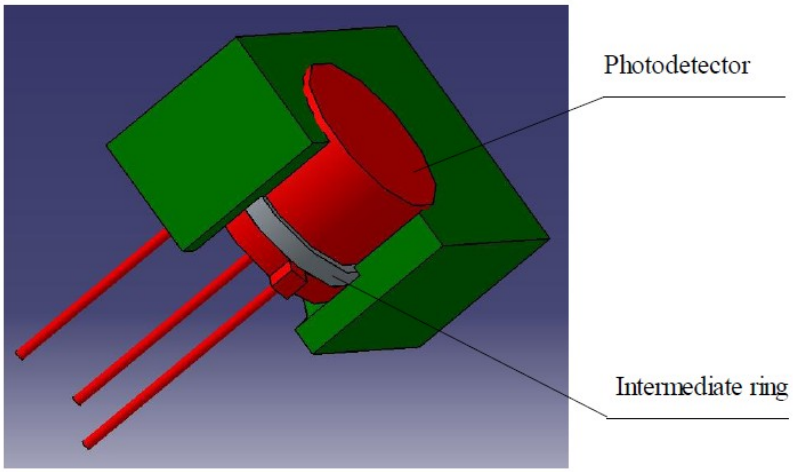

Fig. 3.7 Photodetector mounting scheme

To guarantee detector plane positioning in the focus of the gathering lens some span has to be left for detector axial movement (Fig. 3.8). For this reason an intermediate ring of customized thickness is added to the overall scheme. It is manufactured after exact focusing plane is found. Detector itself is glued to its base.

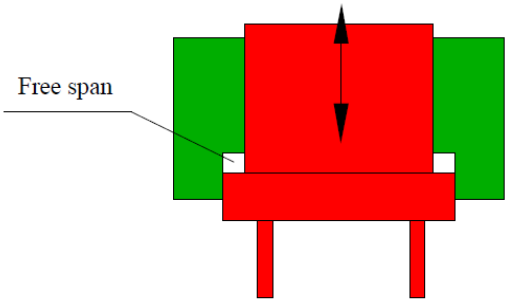

Fig. 3.8 Photodetector positioning scheme

3.2. Mechanical layout.

Mechanical layout contains two main elements:

- double pendulum group;
- piezoactuator group.

Finally all elements are mounted on the common instrument frame (Fig. 3.9).

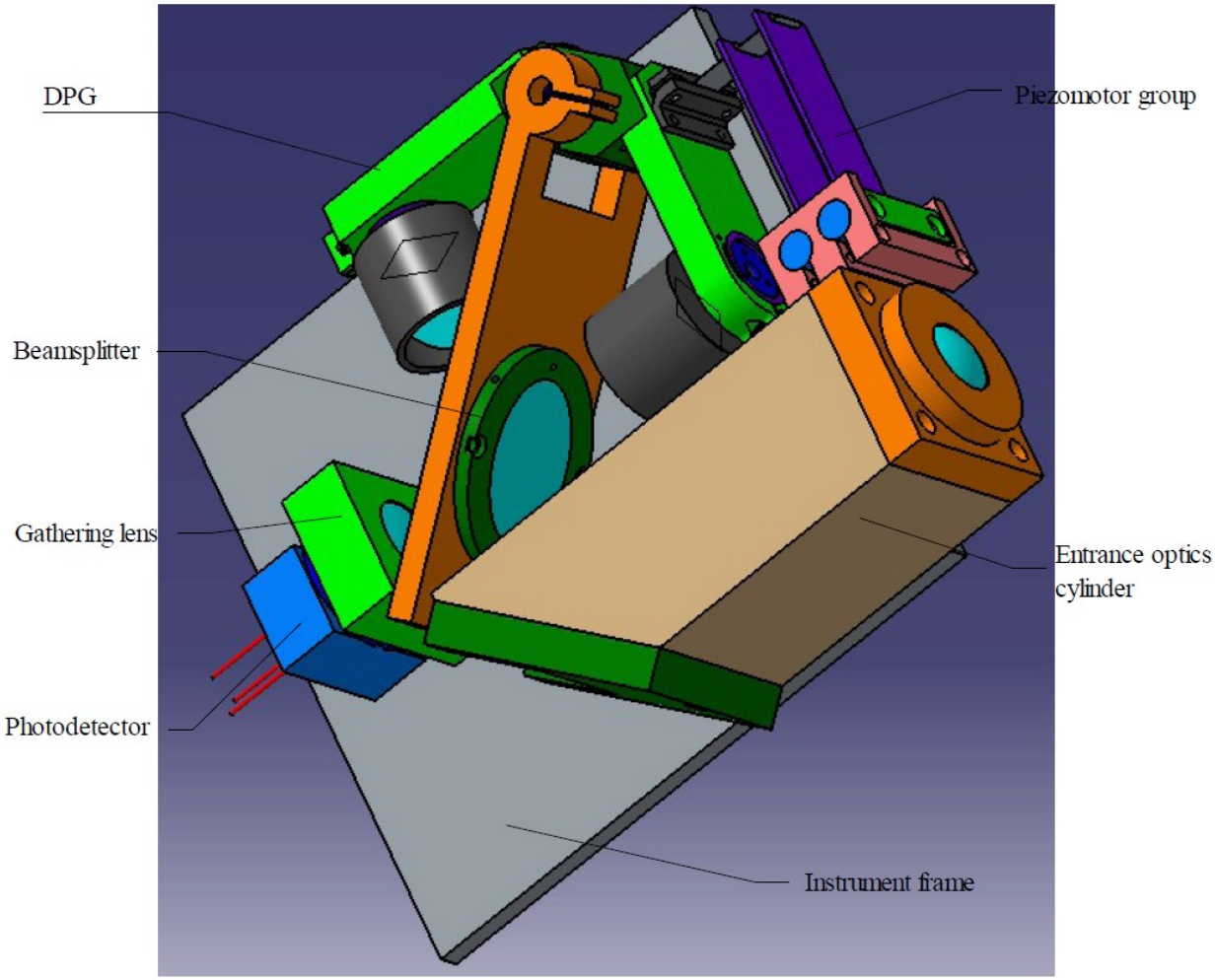

Fig. 3.9. Entire assembly

3.2.1. Piezoactuator group.

Piezoactuator group consists of 2 piezoactuators restrained in the common clamp element mounted on the entrance optics cylinder (Fig. 3.10). With bracket arm it is coupled by an additional support through a steel foil connection.

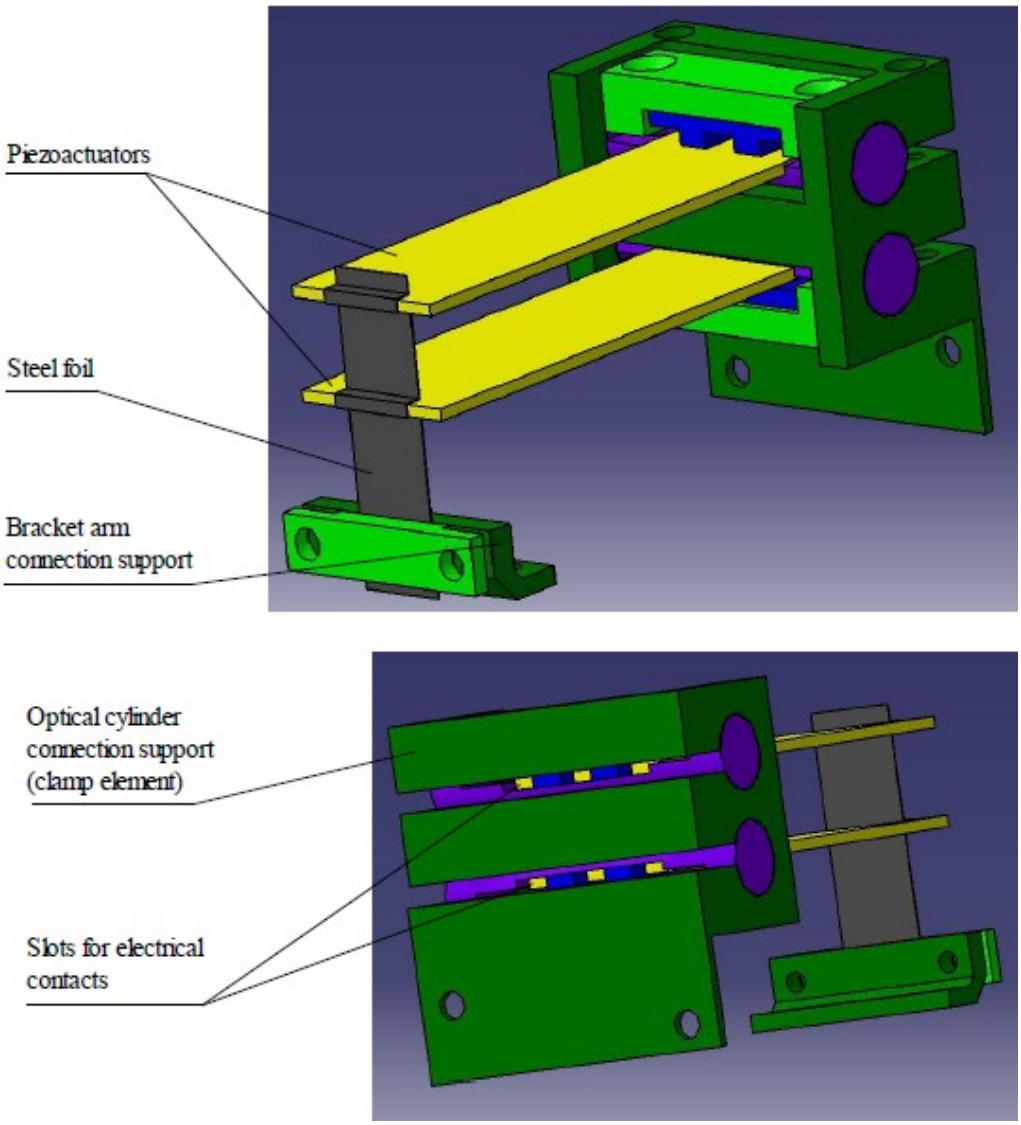

Fig. 3.10 Piezomotor scheme

Clamp element possesses slots for the electrical contacts of actuators.

3.2.2. Double pendulum group.

Double pendulum group represents base for the CCM subgroups (Fig. 3.11). It is mounted using flexural pivots (bearings) [10] and for accuracy reasons uses common base with beamsplitter group.

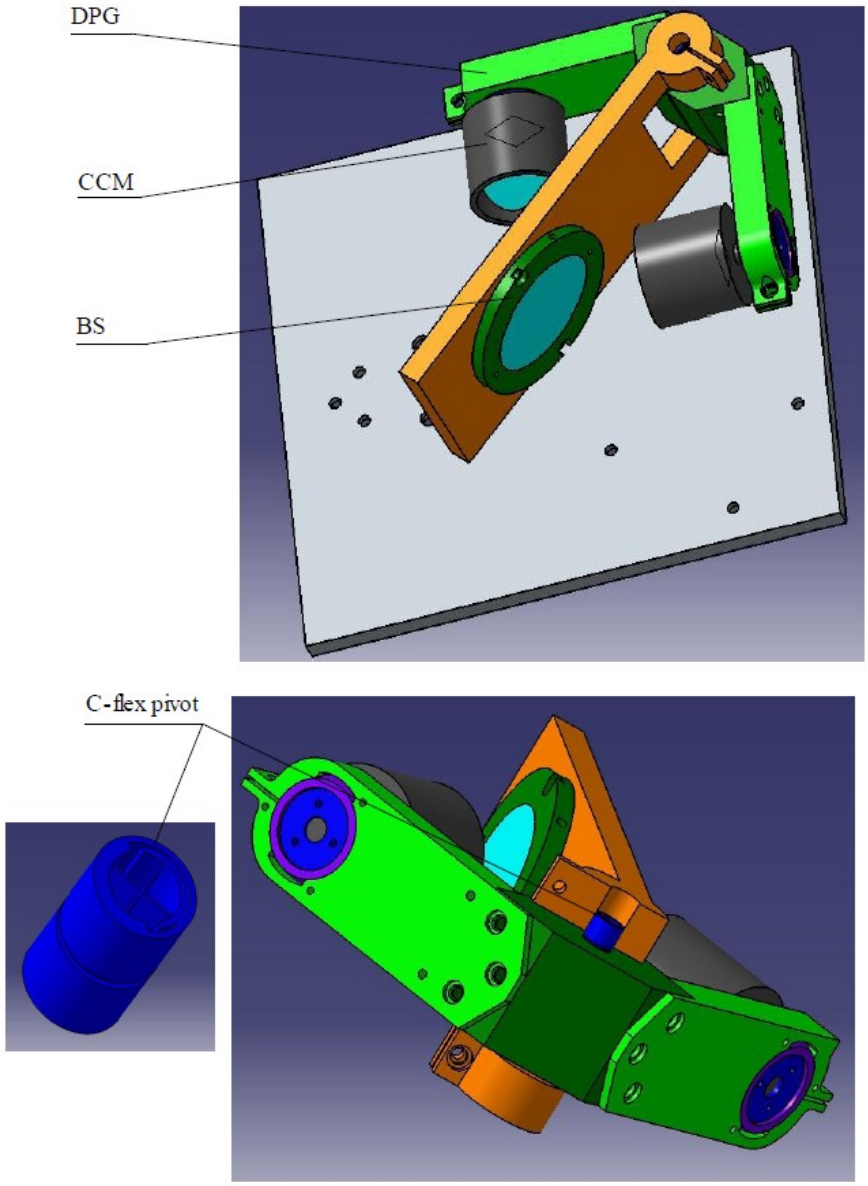

Fig. 3.11 Double pendulum group mounting scheme

3.3 Conclusions

From the developed 3D pattern a set of separate drafts was created to be sent to the factory for manufacturing (see Annex C). Being produced mock up would serve as a trustful model for instrument performance testing as all elements responsible for operating characteristics were elaborated in details

References

[1] "ExoMars Orbiter", Experiment Proposal Information Package, Issue 1 Revision 1, Doc. No: EXM-OM-IPA-ESA-00001, January 2010;

[2] M. Coradini, "The ExoMars Program", July 2009;

[3] "ExoMars Scientific Payload Requirements Document", Issue 1, Rev. 1, Doc. No: EXM-PL-RS-ESA-00001, July 2007;

[4] "Space engineering: Mechanical – Part 3: Mechanisms",ECSS-E-30 Part 3A, April 2000;

[5] M. Kölhed, "MID Infra-red detection strategies in capillary electrophoretic systems", ISBN 91-7155-102-6, 2005;

[6] B. Saggin, E. Alberti, L. Comolli, M. Tarabini, G. Bellucci, S. Fonti "MIMA, a miniaturized infrared spectrometer for Mars ground El exploration: Part III, thermomechanical design", Proc. SPIE 6744, 2007;

[7] B. Saggin, G. Bellucci, L. Comolli, "The planetary fourier spectrometer (PFS) onboard the European Venus Express mission", Planetary and Space Science 54, 2006;

[8] M. J. Puttock, E. G. Thwaite, "Elastic Compression of Spheres and Cylinders at Point and Line Contact", National Standards Laboratory Technical Paper, 2008;

[9] CCM producer datasheet, http://www.plxinc.com/?fuseaction=page&id=193&popup=1;

[10] C-Flex bearings producer datasheet, http://www.c-flex.com/companyproducts.pdf, http://www.c-flex.com/technicaldata.pdf;

[11] Piezo bender actuators producer datasheet, http://www.piceramic.com/datasheet/PL112_PL140_Piezo_Bender_Actuator_Datasheet.pdf;

[12] Photodetector producer datasheet, http://www.calsensors.com/pdf/PIRE_PLUS_DS4.pdf.

Annex A

A.1 Locking mechanism pre dimensioning

A.1.1 Locking force calculations

Going on with calculations presented in the text:

$$F_L = 2 \int_{\Psi_0/2} \int_L N_d \cos\alpha \cos\psi \, d\psi \, R \, dL \quad ,$$

$$F_L = 2 N_d \cos\alpha (\sin(\Psi_0/2) - \sin(0)) \int_L R \, dL \quad ,$$

$$N_d \int_L R \, dL = \frac{F_L}{2\cos\alpha \sin(\Psi_0/2)} \quad ;$$

$$F_{axial} = \int_{\Psi_0} \int_L N_d \sin\alpha \, d\psi \, R \, dL \quad ,$$

$$F_{axial} = \Psi_0 \sin\alpha \, N_d \int_L R \, dL \quad ,$$

$$F_{axial} = \Psi_0 \sin\alpha \frac{F_L}{2\cos\alpha \sin(\Psi_0/2)} \quad ,$$

$$F_{axial} = F_L \tan\alpha \frac{\Psi_0/2}{\sin(\Psi_0/2)} \quad .$$

A.1.2 Pin diameter calculations

Matlab code for minimum pin diameter calculations

```
clc
close all
clear all

F_a = input('input axial force for current alpha');
F_L = 4.2; %[N]
L1 = 10; %[mm]
M = F_L*L1; %[Nm]
d = 0.1; %[mm]
SC = 2; %safety coefficient
sigma_yield = 475; %[MPa]
sigma = 1000; %[MPa]
```

```
while sigma>sigma_yield/SC
   d = d + 0.01;
   W = pi*d^3/32;
   A = pi*d^2/4;
   sigma_b = M/W;
   sigma_c = F_a/A;
   sigma = sigma_b + sigma_c;
end

sigma
d
```

A.1.3 Contact pressure calculations

```
clc
close all
clear all

alpha = input('input cone angle, degrees');
alpha = alpha*pi/180; %[rad]
alpha_dot = alpha*0.95;
E = 7e4; %[MPa]
v = 0.35;
E_dot = E/(2*(1-v^2));
Faxial = input ('input axial force, N');
sigma_yield = 475; %[MPa]
A = 3;
sigma_dot = sigma_yield/A;
a = (E_dot*Faxial/(pi*sin(alpha)*sin(alpha_dot)/sin(alpha –
alpha_dot)/2^0.5*tan(alpha)*sigma_dot^2))^1/2
```

A.2 Piezo actuator calculations

A.2.1 Effect of gravity force

Torque appearing on the brackets due to gravity force (Fig. A.1) neutral position is compensated by preload of flexural bearings.

F_G = mass*0,38g (Mars gravitation amounts 38% of Earth one),
F_G = 0,05 N.

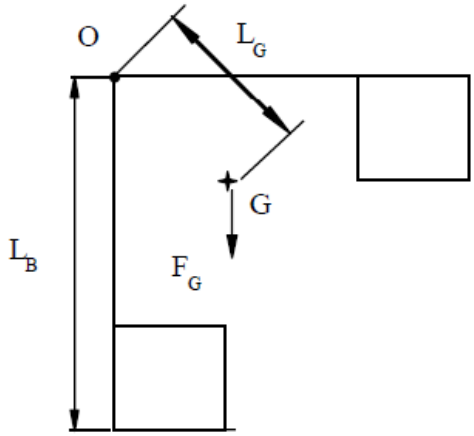

Fig. A.1 Affect of gravity force on pendulum group

$\Sigma M_O = 0$ (neutral position) $\Rightarrow$
$M_{preload\,bearing} = M_{gravity}$,
$M_{preload\,bearing} = \Theta_{preload} * K$ (K = 0,4 Nmm/°),
$M_{gravity} = F_G L_G \cos 45^o$ (L_G = 13 mm).

System being rotated counter-clockwise will undergo the increase of gravity moment, while rotating clockwise – its decrease.

$M_{gravityoperationcondition} = F_G L_G \cos(45^o - \theta_{max})$, (Θ_{max} = 2,5°).

$\Delta M_{gravity} = M_{gravityoperationcondition} - M_{gravity}$,
$\Delta M_{gravity} = F_G L_G (\cos(45^o - \theta_{max}) - \cos 45^o)$ = 0,02 Nmm.

Assuming possible inclinations on Mars (max 45°)
$\Delta M_{gravity} = F_G L_G (\cos(45^o - \theta_{max\,inclination}) - \cos 45^o)$ = 0,19 Nmm.

Considering case without any preload of flexural bearing we obtain:
$\Delta M_{gravity} = F_G L_G \cos(45^o - \theta_{max\,inclination})$ = 0,64 Nmm.

So we consider $\Delta M_{gravityMAX}$ =0,64 Nmm.

A.2.2 Optimal positioning

To find the optimal $L_{actuator}$ (Fig. 2.22) we need to find maximum extremum of function $M_{actuator}$ ($L_{actuator}$), remembering dependence presented on the Fig. A.2.

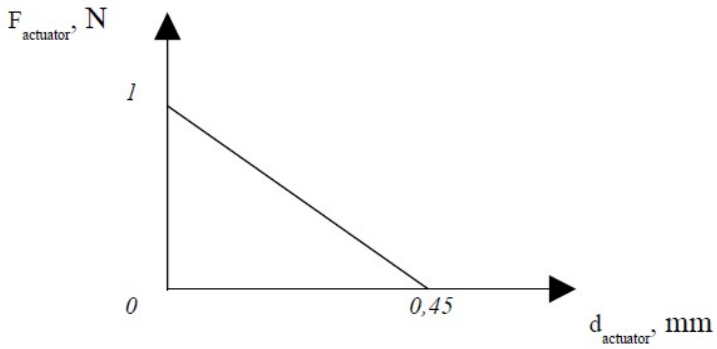

Fig. A.2 PL127.10 actuator force as function of actuator displacement

$M_{actuator} = F_{actuator} * L_{actuator}$;
$F_{actuator} = F_{blocking} * (1 - d_{actuator}/d_{nominal})$,
for PL127.10 $F_{blocking} = 1$ N, $d_{nominal} = 0{,}45$ mm.

$d_{actuator} = d_{pendulum} * L_{actuator}/L_{pendulum}$.

So we can rewrite:

$$M_{actuator} = L_{actuator} F_{blocking} \left(1 - L_{actuator} \frac{d_{pendulum}}{L_{pendulum} d_{nominal}}\right)$$ (Fig A.3)

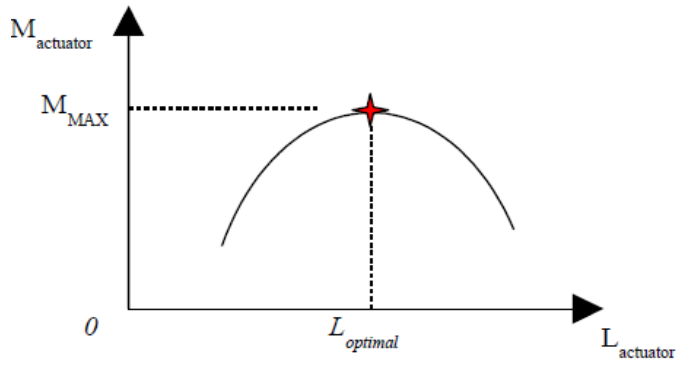

Fig. A.3 PL127.10 actuator moment as function of actuator positioning

$M_{actuator}(L_{optimal}) = M_{MAX}$;

$$\frac{d M_{actuator}}{d L_{actuator}} = 0 \Rightarrow F_{blocking}\left(1 - 2 L_{optimal} \frac{d_{pendulum}}{L_{pendulum} d_{nominal}}\right) = 0 \ ,$$

$$L_{optimal} = \frac{L_{pendulum} d_{nominal}}{2 d_{pendulum}} = 5{,}13\, mm.$$

Annex B

Instrument misalignments calculations

Having measured 3D displacements of characteristic points of optics mounting surfaces (Table B.1) the following matlab code permits to find optics midpoints shifts and mid planes tilts.

Measured displacement	Displacement value, mm	Initial coordinates, mm		
		X	Y	Z
BS_p1_X	0.000101787	86.6885	-38.8258	10.2886
BS_p1_Y	-4.65254e-006			
BS_p1_Z	0.000257248			
BS_p2_X	6.53771e-005	69.9595	-32.3851	-6.44028
BS_p2_Y	4.68832e-006			
BS_p2_Z	0.000132647			
BS_p3_X	4.58432e-005	69.9595	-45.2666	-6.44028
BS_p3_Y	-4.81342e-005			
BS_p3_Z	0.000139794			
L1_p1_X	0.000253713	121.11	-38.8258	-31.2322
L1_p1_Y	-0.000105853			
L1_p1_Z	0.000170342			
L1_p2_X	0.000231436	121.11	-43.2809	-23.9622
L1_p2_Y	-0.000113103			
L1_p2_Z	0.000192952			
L1_p3_X	0.000244998	121.11	-34.3708	-23.9622
L1_p3_Y	-8.90107e-005			
L1_p3_Z	0.000187346			
L2_p1_X	0.000226146	112.361	-38.8258	-28.2322
L2_p1_Y	-9.184e-005			
L2_p1_Z	0.000161943			
L2_p2_X	0.000218063	112.361	-40.6078	-25.3242

L2_p2_Y	-9.4802e-005			
L2_p2_Z	0.000170856			
L2_p3_X	0.000222954			
L2_p3_Y	-8.51877e-005	112.361	-37.0438	-25.3242
L2_p3_Z	0.000168564			
L3_p1_X	0.000161843			
L3_p1_Y	-5.47e-005	83.8606	-38.8258	-32.2322
L3_p1_Z	8.921e-005			
L3_p2_X	0.000132942			
L3_p2_Y	-6.41514e-005	83.8606	-44.1719	-23.5082
L3_p2_Z	0.000115789			
L3_p3_X	0.00014822			
L3_p3_Y	-3.41067e-005	83.8606	-33.4798	-23.5082
L3_p3_Z	0.000109114			
L4_p1_X	3.83371e-006			
L4_p1_Y	-2.3392e-006	58.6676	-38.8258	-7.73218
L4_p1_Z	6.98132e-005			
L4_p2_X	-8.02311e-006			
L4_p2_Y	1.77002e-006	58.6676	-44.1719	0.991762
L4_p2_Z	8.12703e-005			
L4_p3_X	1.01857e-005			
L4_p3_Y	1.07066e-005	58.6676	-34.5832	2.51046
L4_p3_Z	7.35741e-005			
M_p1_X	0.000157356			
M_p1_Y	-5.13981e-005	80.9609	-38.8258	-33.374
M_p1_Z	7.83434e-005			
M_p2_X	0.000119861			
M_p2_Y	-1.27825e-005	72.3642	-32.1056	-24.7773
M_p2_Z	7.68862e-005			
M_p3_X	0.000100601			
M_p3_Y	-5.55592e-005	72.3642	-45.5461	-24.7773
M_p3_Z	8.50866e-005			

RLock_p2_X	4.16831e-005	74.6676	-38.8258	24.8678
RLock_p2_Y	-5.45037e-007			
RLock_p2_Z	0.000310436			
RnoLock_p1_X	0.000215836	101.268	-38.8258	-1.73218
RnoLock_p1_Y	-6.3356e-005			
RnoLock_p1_Z	0.000254954			

Table B.1 Displacements of characteristic points of optics mounting surfaces

```
clc
clear all
close all

%% LENS TELESCOPE%%

% coordinates of lenses - initial
%  p1 p2 p3
% x
% y
% z
L1 = [121.11 121.11 121.11
   -38.8258 -43.2809 -34.3708
   -31.2322 -23.9622 -23.9622];
L2 = [112.361, -38.8258, -28.2322
   112.361, -40.6078, -25.3242
   112.361, -37.0438, -25.3242]';
L3 = [83.8606, -38.8258, -32.2322
   83.8606, -44.1719, -23.5082
   83.8606, -33.4798, -23.5082]';
L4 = [58.6676, -38.8258, -7.73218
   58.6676, -44.1719, 0.991762
   58.6676, -34.5832, 2.51046]';
L=[L1 L2 L3 L4];

% coordinates of displacement of lenses' points
Ld1 = [0.000253713 0.000231436 0.000244998
   -0.000105853 -0.000113103  -8.90107e-005
  0.000170342 0.000192952 0.000187346];
Ld2 = [0.000226146 0.000218063 0.000222954
```

```
  -9.184e-005 -9.4802e-005 -8.51877e-005
   0.000161943 0.000170856 0.000168564];
Ld3 = [0.000161843 0.000132942 0.00014822
   -5.47e-005 -6.41514e-005 -3.41067e-005
   8.921e-005 0.000115789 0.000109114];
Ld4 = [3.83371e-006 -8.02311e-006 1.01857e-005
   -2.3392e-006 1.77002e-006 1.07066e-005
   6.98132e-005 8.12703e-005 7.35741e-005];
Ld=[Ld1 Ld2 Ld3 Ld4];

% coordinates of lenses under thermal stress
%  p1 p2 p3
% x
% y
% z
Lts1 = L1 + Ld1;
Lts2 = L2 + Ld2;
Lts3 = L3 + Ld3;
Lts4 = L4 + Ld4;
Lts=[Lts1 Lts2 Lts3 Lts4];

% vertical displacement of lenses group
%x
lens1_displacement_vertical = sum(Ld1(1,:))/3
lens2_displacement_vertical = sum(Ld2(1,:))/3
lens3_displacement_vertical = sum(Ld3(1,:))/3
lens4_displacement_vertical = sum(Ld4(1,:))/3

% horizontal displacements of lenses group
%y
lens1_displacement_horizontal_y = sum(Ld1(2,:))/3
lens2_displacement_horizontal_y = sum(Ld2(2,:))/3
lens3_displacement_horizontal_y = sum(Ld3(2,:))/3
lens4_displacement_horizontal_y = sum(Ld4(2,:))/3

%z
lens1_displacement_horizontal_z = sum(Ld1(3,:))/3
lens2_displacement_horizontal_z = sum(Ld2(3,:))/3
lens3_displacement_horizontal_z = sum(Ld3(3,:))/3
lens4_displacement_horizontal_z = sum(Ld4(3,:))/3

% lenses tilt calculation
```

```
for i=1:4
   AB = [L(1,2+(i-1)*3)-L(1,1+(i-1)*3) L(2,2+(i-1)*3)-L(2,1+(i-1)*3) L(3,2+
(i-1)*3)-L(3,1+(i-1)*3)];
   AC = [L(1,3+(i-1)*3)-L(1,1+(i-1)*3) L(2,3+(i-1)*3)-L(2,1+(i-1)*3) L(3,3+
(i-1)*3)-L(3,1+(i-1)*3)];
   n(i,:) = AB.*AC;
   a = n(i,:);
   ABts = [Lts(1,2+(i-1)*3)-Lts(1,1+(i-1)*3) Lts(2,2+(i-1)*3)-Lts(2,1+(i-1)*3)
Lts(3,2+(i-1)*3)-Lts(3,1+(i-1)*3)];
   ACts = [Lts(1,3+(i-1)*3)-Lts(1,1+(i-1)*3) Lts(2,3+(i-1)*3)-Lts(2,1+(i-1)*3)
Lts(3,3+(i-1)*3)-Lts(3,1+(i-1)*3)];
   nts(i,:) = ABts.*ACts;
   b = nts(i,:);
   lens_tilt(i) = atan2(norm(cross(a,b)),dot(a,b))*180/pi*360; % *180/pi -
degree; *360 - arc sec
end

lens_tilt %arc sec


%% BEAMSPLITTER %%

% BeamSplitter coordinates
%  p1 p2 p3
% x
% y
% z
BS = [86.6885, -38.8258, 10.2886
69.9595, -32.3851, -6.44028
69.9595, -45.2666, -6.44028]';

BSd = [0.000101787 6.53771e-005 4.58432e-005
   -4.65254e-006 4.68832e-006 -4.81342e-005
   0.000257248 0.000132647 0.000139794];
BSts = BS + BSd;

% Beamsplitter tilt calculation
AB = [BS(1,2)-BS(1,1) BS(2,2)-BS(2,1) BS(3,2)-BS(3,1)];
AC = [BS(1,3)-BS(1,1) BS(2,3)-BS(2,1) BS(3,3)-BS(3,1)];
a = AB.*AC;
ABts = [BSts(1,2)-BSts(1,1) BSts(2,2)-BSts(2,1) BSts(3,2)-BSts(3,1)];
ACts = [BSts(1,3)-BSts(1,1) BSts(2,3)-BSts(2,1) BSts(3,3)-BSts(3,1)];
```

```
b = ABts.*ACts;
bs_tilt = atan2(norm(cross(a,b)),dot(a,b))*180/pi*360 % *180/pi - degree;
*360 - arc sec

%% MIRROR %%

% Mirror coordinates
%  p1 p2 p3
% x
% y
% z
M = [80.9609, -38.8258, -33.374
   72.3642, -32.1056, -24.7773
   72.3642, -45.5461, -24.7773]';
Md = [0.000157356 0.000119861 0.000100601
   -5.13981e-005 -1.27825e-005 -5.55592e-005
   7.83434e-005 7.68862e-005 8.50866e-005];
Mts = M + Md;

% Mirror tilt calculation
AB = [M(1,2)-M(1,1) M(2,2)-M(2,1) M(3,2)-M(3,1)];
AC = [M(1,3)-M(1,1) M(2,3)-M(2,1) M(3,3)-M(3,1)];
a = AB.*AC;
ABts = [Mts(1,2)-Mts(1,1) Mts(2,2)-Mts(2,1) M(3,2)-Mts(3,1)];
ACts = [Mts(1,3)-Mts(1,1) Mts(2,3)-Mts(2,1) Mts(3,3)-Mts(3,1)];
b = ABts.*ACts;
mirror_tilt = atan2(norm(cross(a,b)),dot(a,b))*180/pi*360 % *180/pi - degree;
*360 - arc sec

%% CCM %%

% CCM coordinates
% x y z
CCM1 = [101.268, -38.8258, -1.73218];
CCM2 = [74.6676, -38.8258, 24.8678];
CCMd1 = [4.16831e-005 -5.45037e-007 0.000310436];
CCMd2 = [0.000215836 -6.3356e-005 0.000254954];
CCMts1 = CCM1 + CCMd1;
CCMts21 = CCM2 + CCMd2;

vertical_difference_x = abs(CCMd1(1)-CCMd2(1))
horizontal_difference_z = abs(CCMd1(3)-CCMd2(3))
```

Annex C

Technical drawings

Further are presented technical drawings of particular mock up components:

- beamsplitter holding frame;
- entrance optics telescope;
- double pendulum group main elements.

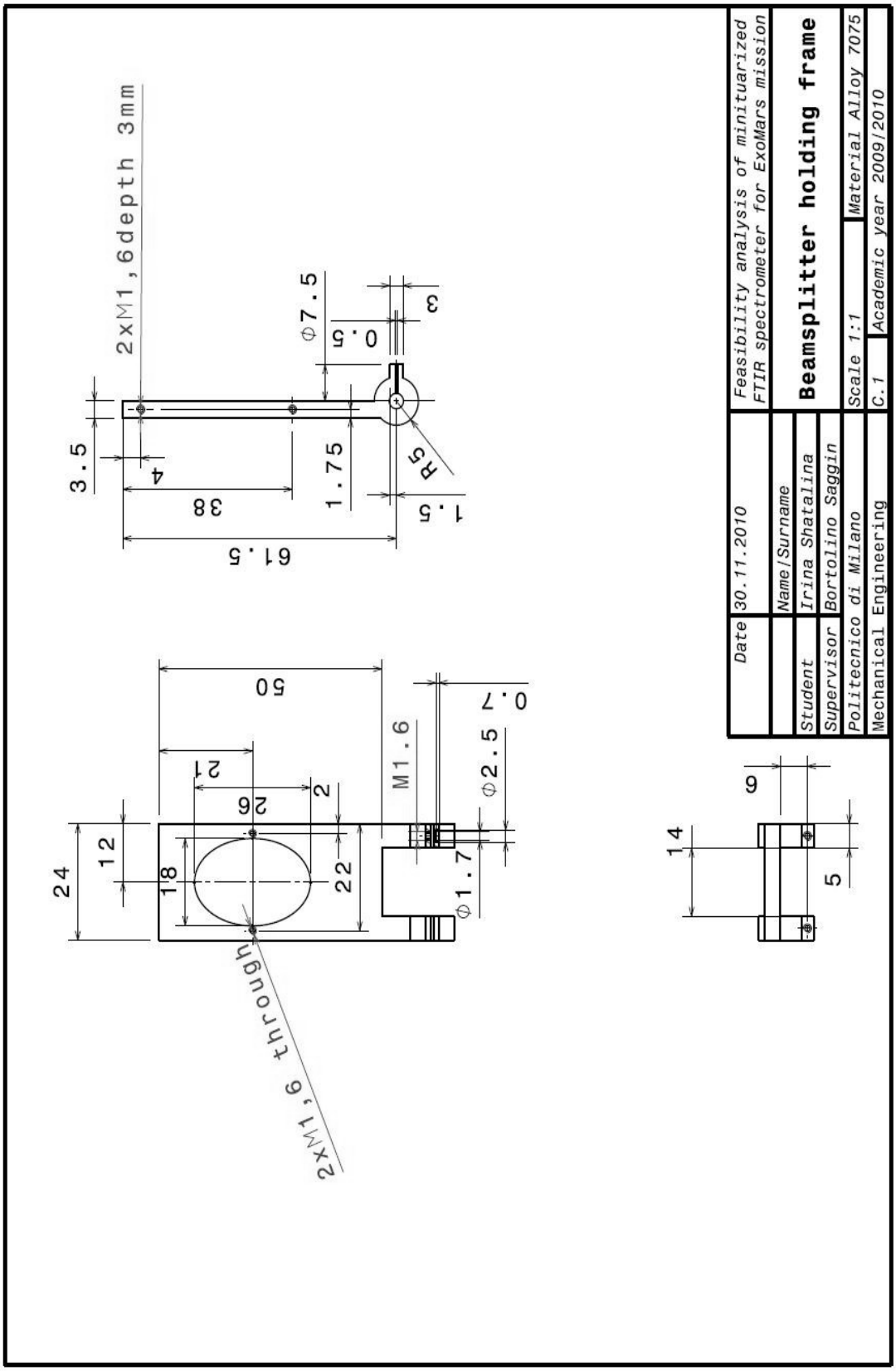
2xM1,6depth 3mm
3.5
4
38
1.75
61.5
φ7.5
0.5
3
R5
1.5
50
21
26
2
M1.6
φ2.5
0.7
24
12
18
22
φ1.7
2xM1,6 through
14
6
5
Feasibility analysis of minituarized FTIR spectrometer for ExoMars mission
Beamsplitter holding frame
Date 30.11.2010
Name/Surname
Student Irina Shatalina
Supervisor Bortolino Saggin
Politecnico di Milano
Mechanical Engineering
Scale 1:1
Material Alloy 7075
C.1
Academic year 2009/2010

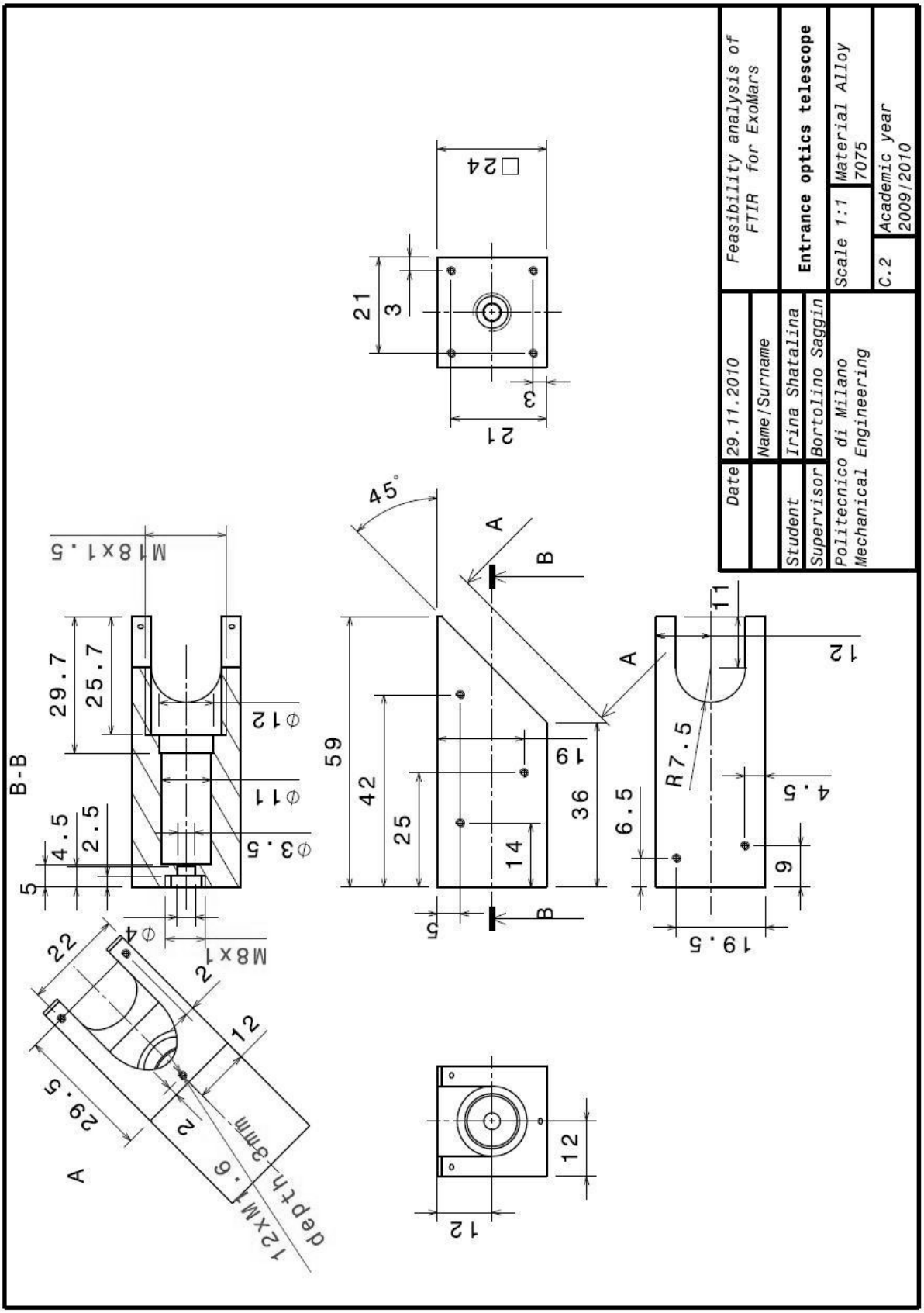
Feasibility analysis of FTIR for ExoMars
Entrance optics telescope
Scale 1:1
Material Alloy 7075
C.2
Academic year 2009/2010
Date 29.11.2010
Name/Surname
Student Irina Shatalina
Supervisor Bortolino Saggin
Politecnico di Milano
Mechanical Engineering
B-B
M18x1.5
M8x1
12xM1.6 depth 3mm
45°
□24
R7.5

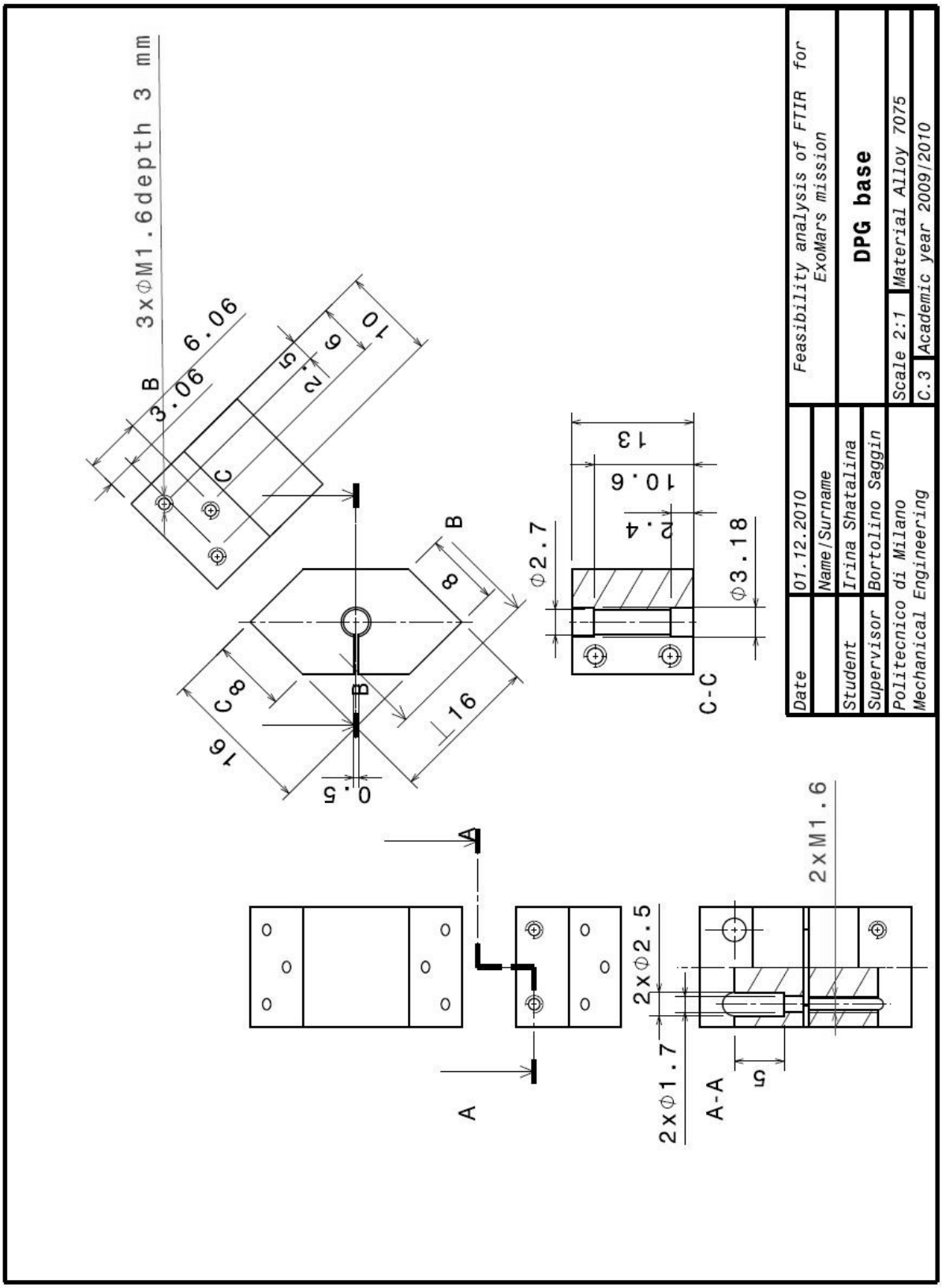
3xΦM1.6depth 3 mm
3.06
6.06
B
C
10
6.5
2
5
B
8
C
8
16
16
0.5
Φ2.7
13
10.6
2.4
Φ3.18
C-C
A
A
2xM1.6
2xΦ2.5
2xΦ1.7
A-A
5
Feasibility analysis of FTIR for ExoMars mission
DPG base
Date
01.12.2010
Name/Surname
Student
Irina Shatalina
Supervisor
Bortolino Saggin
Politecnico di Milano
Mechanical Engineering
Scale 2:1
Material Alloy 7075
C.3
Academic year 2009/2010

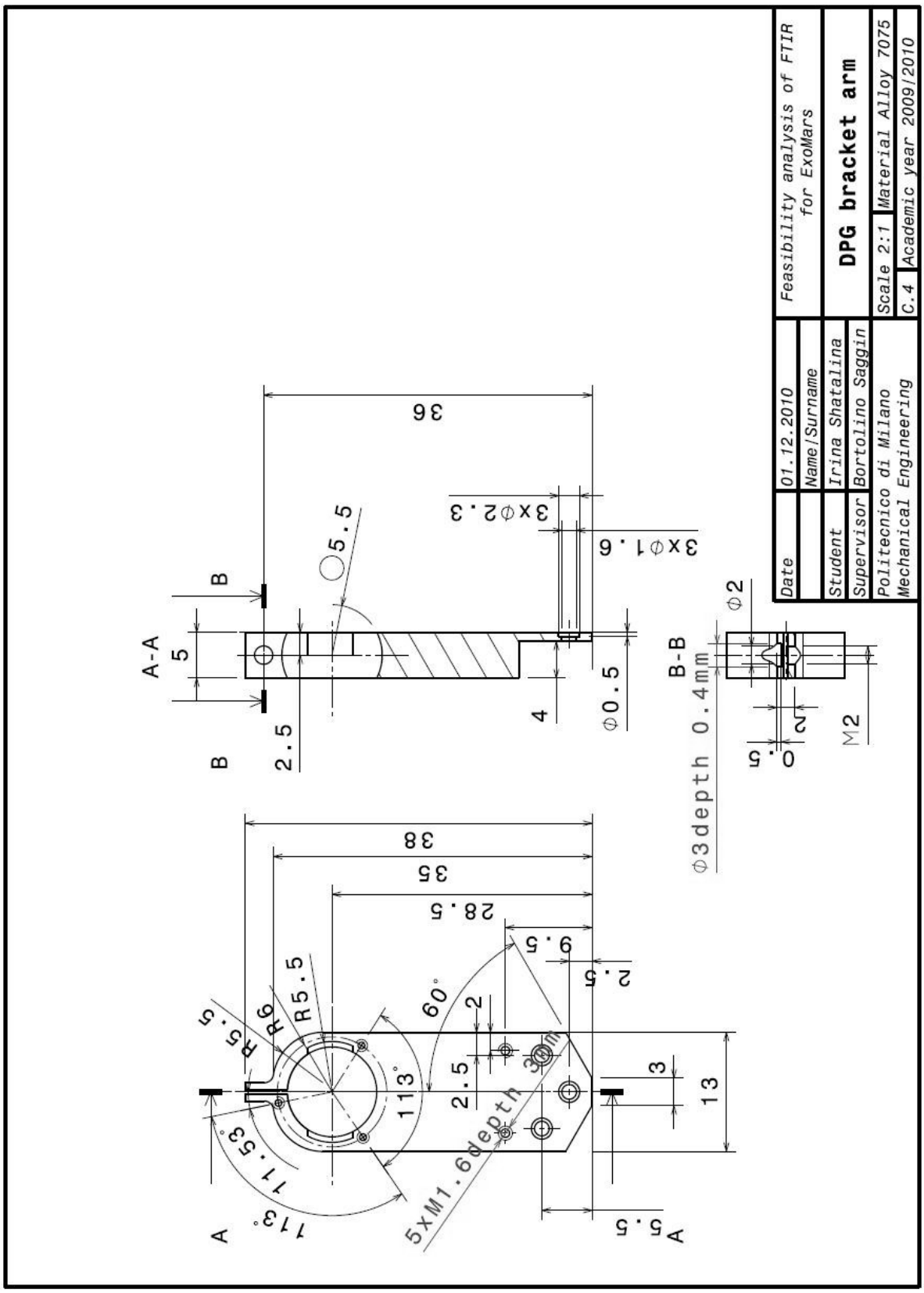
Feasibility analysis of FTIR for ExoMars
DPG bracket arm
Scale 2:1
Material Alloy 7075
C.4
Academic year 2009/2010
Date
01.12.2010
Name/Surname
Student
Irina Shatalina
Supervisor
Bortolino Saggin
Politecnico di Milano
Mechanical Engineering
A-A
B-B
36
38
35
28.5
9.5
2.5
5
2
3
13
5.5
4
2.5
R5.5
R9.5
60°
113°
11.53°
5xM1.6depth 3mm
Φ3depth 0.4mm
Φ2
M2
Φ0.5
3xΦ2.3
3xΦ1.6